Chemical-substitution-driven giant anomalous Hall and Nernst effects in magnetic cubic Heusler compounds

Guangzong Xing[a,*], Keisuke Masuda[a,b,*], Terumasa Tadano[a,b] and Yoshio Miura[a,b]

[a]Research Center for Magnetic and Spintronic Materials, National Institute for Materials Science, Tsukuba, Ibaraki, 305-0047, Japan
[b]Digital Transformation Initiative Center for Magnetic Materials, National Institute for Materials Science, Tsukuba, Ibaraki, 305-0047, Japan

ARTICLE INFO

Keywords:
Anomalous Hall conductivity
Anomalous Nernst conductivity
Heusler compounds
High-throughput screening

Abstract

Chemical substitution efficiently optimizes the physical properties of Heusler compounds, especially their anomalous transport properties, including anomalous Hall conductivity (AHC) and anomalous Nernst conductivity (ANC). This study systematically investigates the effect of chemical substitution on AHC and ANC in 1493 magnetic cubic Heusler compounds using high-throughput first-principles calculations. Notable trends emerge in Co- and Rh-based compounds, where chemical substitution effectively enhances the AHC and ANC. Intriguingly, certain chemically substituted candidates exhibit outstanding enhancement in AHCs and ANCs, such as $(Co_{0.8}Ni_{0.2})_2FeSn$ with considerable AHC and ANC values of -2567.78 S cm^{-1} and 8.27 A m^{-1}K^{-1}, respectively, and $(Rh_{0.8}Ru_{0.2})_2MnIn$ with an AHC of 1950.49 S cm^{-1}. In particular, an extraordinary ANC of 8.57 A m^{-1}K^{-1} is identified exclusively in $Rh_2Co_{0.7}Fe_{0.3}In$, nearly double the maximum value of 4.36 A m^{-1}K^{-1} observed in the stoichiometric Rh_2CoIn. A comprehensive band structure analysis underscores that the notable enhancement in ANC arises from the creation and modification of the energy-dependent nodal lines through chemical substitution. This mechanism generates a robust Berry curvature, resulting in significant ANCs. These findings emphasize the pivotal role of chemical substitution in engineering high-performance materials, thereby expanding the horizons of transport property optimization within Heusler compounds.

1. Introduction

Ever since the discovery of the Seebeck effect in 1826 [1], considerable efforts have been directed toward improving the performance of conventional thermoelectric devices. The Seebeck effect, known as the longitudinal thermoelectric effect, involves the generation of an electric field parallel to the applied temperature gradient. In general, complex device structures are typically required to enhance thermoelectric performance. In recent years, transverse thermoelectric devices driven by the anomalous Nernst effect (ANE) have gained increased interest due to their inherent simplicity [2, 3].

The ANE serves as the thermoelectric counterpart to the anomalous Hall effect (AHE), wherein a transverse electric field is generated when a perpendicular temperature gradient is applied in the absence of the external magnetic filed [4]. Similarly, the AHE describes the generation of a transverse electric field in response to the electric field along the perpendicular direction [5]. The linear response coefficients of these effects, known as the anomalous Hall conductivity (AHC) and anomalous Nernst conductivity (ANC), originate from two primary contributions: extrinsic and intrinsic. Extrinsic contributions are related to the electron scattering by impurities, whereas the intrinsic component of AHC and ANC purely originates from the electronic structure, driven by the summation of the Berry curvature (BC) within the first Brillouin zone (FBZ) [6, 7]. These anomalous transport behaviors are commonly observed in magnetic materials, where a robust BC is induced through breaking the time-reversal symmetry, driven by the Weyl points or nodal lines (NL) with nontrivial topological characteristics [8–15].

Among various categories of magnetic materials, Heusler compounds of $L2_1$ type are of great interest. They exhibit promising properties for various applications, such as high spin polarization [16], high Curie temperature [17], novel shape-memory [18, 19] effect and notable magnetocaloric effect [20]. Remarkably, the intriguing anomalous transport properties of these materials have been extensively investigated by both experimental analysis and first-principles calculations based on density functional theory (DFT) [21–23]. Theoretical work by Noky *et al*. [24, 25] focused on Co- and Fe-based Heusler compounds and revealed the vital role of mirror symmetry-protected NLs in generating substantial AHC and ANC. It is important to note that the mirror symmetry of $L2_1$-type Heusler compounds causes the sum of BCs induced by gapless NLs to cancel out, resulting in zero AHC and ANC. However, the NL becomes gapped when mirror symmetry is broken by a small perturbation such as the spin-orbit coupling (SOC). Consequently, strong BC is induced in the gapped NLs, leading to a large AHC and ANC. For instance, in the ferromagnetic Co_2MnGa, several research groups have reported a large ANC of $\sim$4 A m^{-1}K^{-1} at 300 K, accompanied by a considerable AHC with the magnitude of 10^3 S cm^{-1} [13, 26, 27]. The presence of NL and Weyl points near the Fermi energy in Co_2MnGa was confirmed by the angle-resolved photoemission spectroscopy and the first-principles calculations [13, 22, 26, 28].

XING.Guangzong@nims.go.jp (G. Xing); MASUDA.Keisuke@nims.go.jp (K. Masuda)
ORCID(s): 0000-0002-8299-8585 (G. Xing); 0000-0002-6884-6390 (K. Masuda); 0000-0002-8132-2161 (T. Tadano); 0000-0002-5605-5452 (Y. Miura)

Theoretical investigation of anomalous transport properties has focused mainly on stoichiometric materials. However, it is important to recognize that chemical substitution offers a promising way to tailor these properties, and the effectiveness of enhancing AHC and ANC through chemical substitution has been observed in various experimental studies. Shen *et al*. [29] reported an enhanced AHC in $(Co,Ni)_3Sn_2S_2$ alloy. Increased ANC was observed in $Co_2Mn(Al,Si)$ and $Co_2(Ti,V)Sn$ alloys [30, 31]. Previous theoretical studies have mainly focused on stoichiometric compounds and estimated the effect of chemical substitution using the band-filling approach [32], which fails to encompass electronic structure changes due to chemical substitution. To directly understand the chemical substitution effect on anomalous transport properties of a wide range of compounds, employing first-principle high-throughput calculations becomes imperative. Noky *et al*. [33] performed a comprehensive study on the anomalous transport properties in magnetic cubic Heusler compounds and identified potential candidates with significant AHC and ANC. However, their study did not directly consider the influence of chemical substitution on AHC and ANC. To date, there is a notable absence of comprehensive studies that directly address the effect of chemical substitution on the anomalous transport properties in Heusler compounds.

In response, a comprehensive high-throughput approach is employed in our study to directly explore the effect of chemical substitution on AHC and ANC in Heusler compounds. The AHC and ANC are computed using the tight-binding Hamiltonian by automatically constructing the maximally localized Wannier functions. Our study encompasses a vast data set of 1493 compounds derived from 104 stoichiometric mother compounds with potential AHC or ANC, as reported by Noky *et al*.[33]. Chemical substitution is treated using virtual crystal approximation (VCA), a conventional method commonly employed for various properties in magnetic materials [34–37]. Within the VCA framework, a virtual element, denoted as $X_{1-x}X'_x$, is employed, where X and X' represent the original element and its substitution, respectively, with x indicating the concentration of the substitution. This approach ensures the preservation of the symmetry between the investigated candidates and their corresponding stoichiometric counterparts. Furthermore, the justification for the use of VCA to maintain symmetry is supported by experimental observations of the $L2_1$ order in off-stoichiometric Co_2MnAl, confirmed by x-ray fluorescence analysis in certain cases of chemical substitution with Si [30]. Our study identified a substantial number of Heusler compounds with chemical substitution that exhibited enhanced AHC and ANC. Notably, a series of chemically substituted compounds showcase ANC values at the Fermi energy surpassing peak values in their respective stoichiometric mother compounds. This originates from a significant change in the electronic structure due to chemical substitution. Of particular interest is the nearly twofold increase in ANC in $Rh_2Co_{0.7}Fe_{0.3}In$, reaching 8.57 $A\,m^{-1}K^{-1}$ at 300 K, compared to the peak value in the Rh_2CoIn (4.36 $A\,m^{-1}K^{-1}$). The band structure analysis underscores the crucial role of chemical substitution in creating or modifying the NLs, ultimately leading to significant enhancements in both AHC and ANC.

2. Computational method

2.1. Description of the workflow

Figure 1(b) illustrates the workflow of the high-throughput calculation, where transport properties were automatically computed using the in-house-developed Python scheme linked to Quantum Espresso (QE), Wannier90, and Wanniertools software. The initial stoichiometric compounds were selected from the database of Noky *et al*. [33] based on the maximum of AHC or ANC ($T = 300$ K) in the energy window of 0.25 eV around the Fermi energy, ensuring a threshold of 700 $S\,cm^{-1}$ and 3 $A\,m^{-1}K^{-1}$, respectively. In total, 104 compounds were selected, comprising 98 $L2_1$-type (space group $Fm\bar{3}m$, # 225) and 6 inverse (space group $F\bar{4}3m$, # 216) compounds, [see Fig. 1(a)] respectively. Three types of Heusler compounds with chemical substitution, characterized by the chemical formula $(X_{1-x}X'_x)_2YZ$, $X_2Y_{1-x}Y'_xZ$ and $X_2YZ_{1-x}Z'_x$, were simulated using VCA, where X' (Y', Z') is the neighbor element of X (Y, Z) and $x = 0$, 0.1, 0.2, 0.3, respectively. In $L2_1$-type Heusler structures, the $X_{1-x}X'_x$, $Y_{1-x}Y'_x$, and $Z_{1-x}Z'_x$ atoms occupy the Wyckoff positions 8*c* (1/4, 1/4, 1/4), 4*a* (0, 0, 0), and 4*b* (1/2, 1/2, 1/2), respectively. However, in the inverse Heusler structures, half of the 8*c* $X_{1-x}X'_x$ atoms are replaced by the 4*a* $Y_{1-x}Y'_x$ atom, and the Wyckoff positions are redefined as $X_{1-x}X'_x$ [4*a* (0, 0, 0)], $X_{1-x}X'_x$ [4*c* (1/4, 1/4, 1/4)], $Y_{1-x}Y'_x$ [4*d* (3/4, 3/4, 3/4)], and $Z_{1-x}Z'_x$ [4*b* (1/2, 1/2, 1/2)], respectively. A total of 1528 candidates were generated as input for this comprehensive study.

Here, all investigated candidates were considered to be in collinear ferromagnetic or ferrimagnetic states, and as such, the initial magnetization was aligned along the [001] Cartesian crystal axis. The criteria used to assess the energy difference, denoted as

$$\Delta\epsilon = \sqrt{\frac{1}{N_{n,\boldsymbol{k}}}\sum_{n,\boldsymbol{k}}(\epsilon^{\mathrm{DFT}}_{n,\boldsymbol{k}} - \epsilon^{\mathrm{Wan}}_{n,\boldsymbol{k}})^2} \tag{1}$$

where $\epsilon^{\mathrm{DFT}}_{n,\boldsymbol{k}}$ and $\epsilon^{\mathrm{Wan}}_{n,\boldsymbol{k}}$ denote the eigenenergy obtained by QE and Wannier90 codes, respectively. n and $\boldsymbol{k}$ represent the band index and Bloch wave vector, respectively. The energy of $\epsilon^{\mathrm{DFT}}_{n,\boldsymbol{k}}$ ($\epsilon^{\mathrm{Wan}}_{n,\boldsymbol{k}}$) obtaining $\Delta\epsilon$ is constrained to be lower than $\epsilon_{\mathrm{F}} + 1$ eV, where ϵ_{F} represents the Fermi energy. $N_{n,\boldsymbol{k}}$ is the total number of points at each n and $\boldsymbol{k}$ within the defined energy range. The largest $\Delta\epsilon$ of 2.02 meV was observed in $Fe_2ScAl_{0.9}Si_{0.1}$. As shown in Fig. S1 of the Supplemental Material (SM), an almost perfect match of the band structure obtained from DFT calculations and Wannierization suggests that the applied threshold of ∼2 meV is reasonable to obtain accurate AHCs and ANCs. Subsequently, all candidates were adopted to the workflow

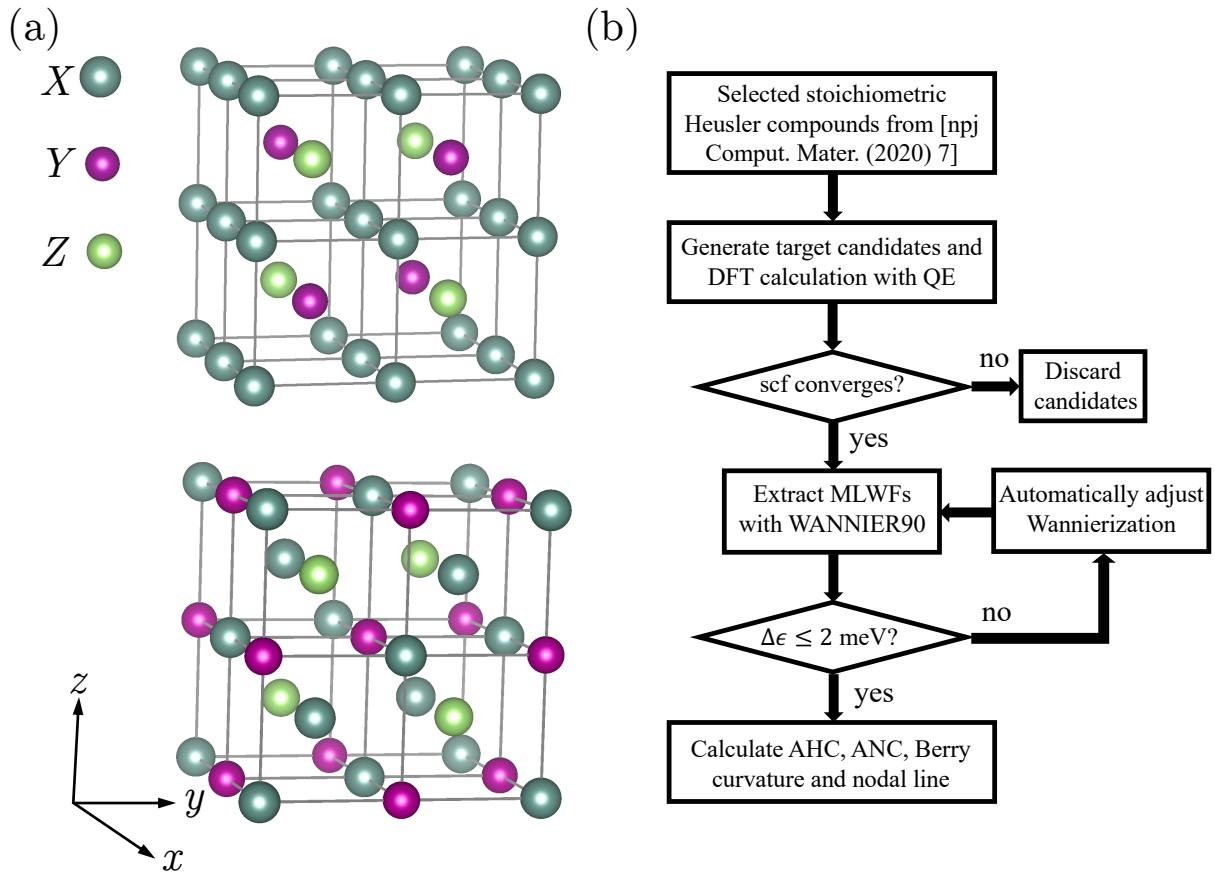

Figure 1: (a) Crystal structure of the $L2_1$-type (upper panel) and inverse (lower panel) Heusler compounds, respectively. (b) Workflow for the present high-throughput screening. The initial stoichiometric mother compounds were selected from Ref. [33] based on the maximum values of σ_{xy} or α_{xy}, which are larger than or equal to 700 S cm^{-1} and 3 A m^{-1}K^{-1}, respectively.

and the AHC and ANC were calculated if the aforementioned criteria were met. As a result, a success rate of ∼98% (1493 candidates) was achieved in this investigation.

2.2. Intrinsic contribution to the AHC and ANC

The second-rank antisymmetric AHC tensor can be described as a pseudovector $\boldsymbol{\sigma} = (\sigma_{yz}, \sigma_{xz}, \sigma_{xy})$, whose shape is associated with the direction of the magnetization. All examined candidates, including $L2_1$-type and inverse Heusler compounds, belong to the magnetic Laue group $4/mm'm'$, where prime denotes time-reversal symmetry, when the magnetization is oriented along the [001] direction [38–40]. Constrained by the pseudovector transformation under the symmetry, only σ_{xy} remains nontrivial in this context [32, 41, 42].

The intrinsic component of anomalous Hall conductivity σ_{xy}, which arises solely from the electronic band structure, can be directly evaluated using the Kubo formula [5, 43],

$$\sigma_{xy} = -\frac{e^2}{\hbar}\int_{\mathrm{BZ}}\frac{d\boldsymbol{k}}{(2\pi)^3}\sum_n f(\epsilon_{n\boldsymbol{k}})\Omega_{n,xy}(\boldsymbol{k}). \tag{2}$$

Here, $\hbar$, e, and $\epsilon_{n\boldsymbol{k}}$ represent the reduced Planck constant, positive elementary charge, and eigenenergy. The Fermi distribution function is denoted by $f(\epsilon) = (\mathrm{e}^{(\epsilon-\mu)/k_{\mathrm{B}}T}+1)^{-1}$, where μ stands for the chemical potential. The Berry curvature $\Omega_{n,xy}(\boldsymbol{k})$ for band n, which can be expressed as,

$$\Omega_{n,xy}(\boldsymbol{k}) = -2\hbar^2\mathrm{Im}\sum_{m(\neq n)}\frac{\langle n\boldsymbol{k}|\hat{v}_x|m\boldsymbol{k}\rangle\langle m\boldsymbol{k}|\hat{v}_y|n\boldsymbol{k}\rangle}{(\epsilon_{n\boldsymbol{k}}-\epsilon_{m\boldsymbol{k}})^2}, \tag{3}$$

with $\hat{v}_x$ ($\hat{v}_y$) being the k_x (k_y) component of the velocity operator, and $|n\boldsymbol{k}\rangle$ representing the eigenstate.

Similarly, the anomalous Nernst conductivity α_{xy} can be obtained by integrating the BC over the first Brillouin zone with a different occupation function. It can be expressed as [35, 44],

$$\alpha_{xy} = \frac{ek_{\mathrm{B}}}{\hbar}\int_{\mathrm{BZ}}\frac{d\boldsymbol{k}}{(2\pi)^3}\sum_n s(\epsilon_{n\boldsymbol{k}})\Omega_{n,xy}(\boldsymbol{k}), \tag{4}$$

where $s(\epsilon) = -f(\epsilon)\ln f(\epsilon) - [1-f(\epsilon)]\ln[1-f(\epsilon)]$ is the density entropy function, and k_{B} denotes the Boltzmann constant. As proposed by Xiao *et al.*, α_{xy} can be connected with σ_{xy} through integration by parts, which is written

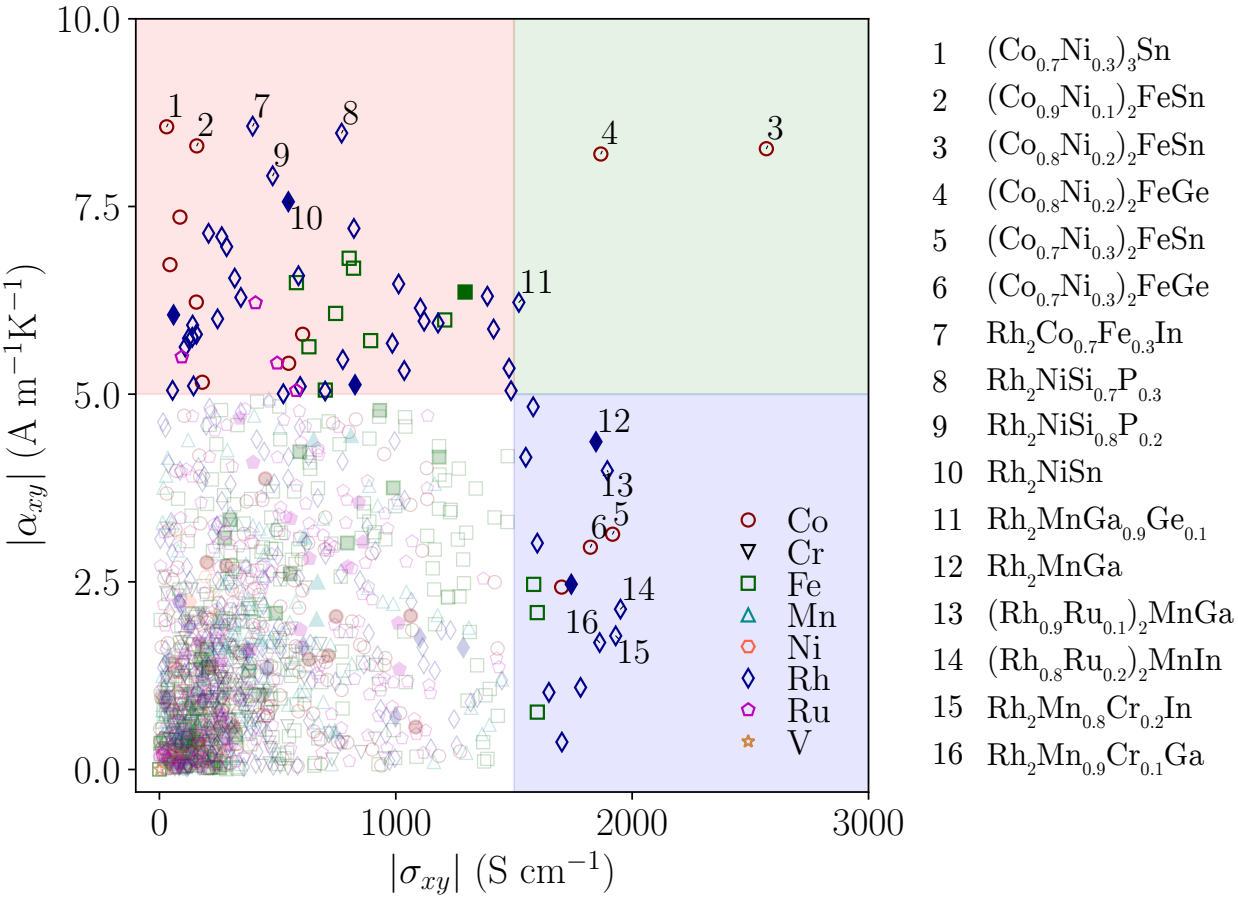

Figure 2: Absolute value of σ_{xy} (at $T = 0$ K) and α_{xy} (at $T = 300$ K) for investigated Heusler compounds (1493 in total). Filled and open symbols with the same color represent stoichiometric and chemically substituted compounds containing the same element at the X site. The red and blue areas indicate candidates with large $|\sigma_{xy}|$ and $|\alpha_{xy}|$, respectively, while the green area involves the candidates that possess both large $|\sigma_{xy}|$ and $|\alpha_{xy}|$.

as [45],

$$\alpha_{xy} = \frac{1}{eT}\int d\epsilon\ (\epsilon - \mu)\frac{\partial f}{\partial \epsilon}\sigma_{xy}(\epsilon, T = 0) \tag{5}$$

2.3. Computational details

We perform first-principles calculations of the electronic band structure using the Quantum ESPRESSO code [46, 47], where the generalized gradient approximation (GGA), proposed by Perdew, Burke, and Ernzerhof (PBE) [48], was adopted. The fully relativistic optimized normal-conserving Vanderbilt (ONCV) peudopotentials [49] taken from the PseudoDojo [50] were employed. Spin-orbit coupling was included for all transport quantity and BC calculations. A kinetic cutoff of 100 and 400 Ry was chosen for the wave function and charge density, respectively. For self-consistent calculation, a k-point mesh density of $\sim$450 Å^3 was employed, with a total energy convergence criterion of 10^{-10} Ry. We adopted the same lattice parameters as those reported in Ref. [33] for both the chemically substituted Heusler alloys and their corresponding stoichiometric counterparts to compare the results.

The σ_{xy} was calculated based on the maximally localized Wannier function (MLWF) using the Wannier90 code [51, 52]. The tight-binding Hamiltonian was obtained from first-principles calculations with a uniform $10 \times 10 \times 10$ k-mesh. To construct the MLWF, we employ the selected columns of the density matrix (SCDM) method [53–55], which is well-suited for high-throughput calculations. SCDM requires only two free parameters, automatically determined in our Python scheme. The outer energy window is automatically adjusted in the disentanglement procedure until $\Delta\epsilon$ reaches the defined criterion. For detailed parameters of Wannierization, please refer to the SM. The σ_{xy} was computed using a $150 \times 150 \times 150$ k-mesh in the FBZ. A denser k-mesh of $200 \times 200 \times 200$ was used for Co_2MnGa and a change of σ_{xy} within $\sim$1% was observed, suggesting that the current k-mesh was dense enough. α_{xy} was evaluated using Equation (5) within the energy range of $[-0.4:0.4]$ eV with respect to the Fermi energy at 300 K. The BC and nodal line network of the selected candidates were analyzed using wanniertools software [56].

Table 1
Identified top 10 promising $L2_1$-type candidates with large $|\sigma_{xy}|$ (at $T = 0$ K) at the Fermi energy.

Candidates	SG	m (μ_B/f.u.)	σ_{xy} (S cm^{-1})	α_{xy} (A m^{-1}K^{-1})	$\sigma_{xy}^{\max}$ [$\Delta\epsilon$] (S cm^{-1}) [(eV)]	$\alpha_{xy}^{\max}$ [$\Delta\epsilon$] (A m^{-1}K^{-1}) [(eV)]
$(Co_{0.8}Ni_{0.2})_2FeSn$	225	5.33	−2567.78	8.27	−3224.09 (0.02)	11.99 (−0.03)
$(Rh_{0.8}Ru_{0.2})_2MnIn$	225	3.95	1950.49	−2.14	1950.49 (0.00)	−6.67 (−0.05)
$(Rh_{0.9}Ru_{0.1})_2MnGa$	225	3.94	1894.95	−3.98	2148.66 (0.04)	−7.09 (−0.07)
$(Co_{0.8}Ni_{0.2})_2FeGe$	225	5.31	−1867.45	8.20	−3152.20 (0.02)	10.90 (−0.03)
Rh_2MnAl	225	4.11, 4.1[a]	1742.50, 1723[a]	2.47, 2.26[a]	2027.10 (−0.04)	5.97 (0.09)
$Co_2Mn_{0.9}Fe_{0.1}Ga$	225	4.20	1701.59	2.43	1701.59 (0.00)	5.15 (0.04)
$(Fe_{0.8}Mn_{0.2})_2MnSn$	225	6.50	1598.79	0.76	1623.15 (−0.01)	4.04 (0.06)
$(Fe_{0.9}Mn_{0.1})_2CoIn$	225	7.08	1583.29	2.47	1646.07 (−0.01)	7.27 (0.07)
$Fe_2ScIn_{0.8}Sn_{0.2}$	225	3.98	1473.78	−4.17	1769.44 (0.13)	5.63 (0.16)
$(Fe_{0.8}Mn_{0.2})_3Sn$	225	7.15	1472.18	3.30	1787.16 (−0.03)	5.01 (0.04)

[a]Theoretical results obtained with VASP, Ref. [33]
The full results are tabulated in the Supplemental Material. Contents in the table are the space group (SG), calculated magnetic moment m per formula unit, the σ_{xy} and α_{xy} at the Fermi energy, and the maximum value $\sigma_{xy}^{\max}$ and $\alpha_{xy}^{\max}$ obtained in an energy range of $[-0.3:0.3]$ eV around the Fermi energy. $\Delta\epsilon$ denotes the energy difference of the maximum values with respect to the Fermi energy.

Table 2
Identified top 10 promising $L2_1$-type candidates with large $|\alpha_{xy}|$ (at $T = 300$ K) at the Fermi energy.

Candidates	SG	m (μ_B/f.u.)	σ_{xy} (S cm^{-1})	α_{xy} (A m^{-1}K^{-1})	$\sigma_{xy}^{\max}$ [$\Delta\epsilon$] (S cm^{-1}) [(eV)]	$\alpha_{xy}^{\max}$ [$\Delta\epsilon$] (A m^{-1}K^{-1}) [(eV)]
$Rh_2Co_{0.7}Fe_{0.3}In$	225	3.43	394.57	8.57	−1649.50 (0.10)	9.74 (0.03)
$(Co_{0.7}Ni_{0.3})_3Sn$	225	3.15	−30.66	8.56	−2614.20 (0.06)	11.48 (0.03)
$Rh_2NiSi_{0.7}P_{0.3}$	225	0.92	−770.92	8.48	−1595.03 (0.06)	8.79 (−0.02)
$(Co_{0.9}Ni_{0.1})_2FeSn$	225	5.59	−158.04	8.31	−3351.26 (0.10)	12.65 (0.04)
$(Co_{0.8}Ni_{0.2})_2FeGe$	225	5.31	−1867.45	8.20	−3152.20 (0.02)	10.90 (−0.03)
Rh_2NiSn	225	1.15, 1.0[a]	−545.48, −360[a]	7.56, 8.14[a]	−1728.71 (0.14)	7.56 (0.00)
$(Co_{0.8}Ni_{0.2})_2MnP$	225	5.84	86.84	7.36	−1548.89 (0.12)	8.41 (0.03)
$Rh_2Co_{0.7}Fe_{0.3}Ga$	225	3.44	284.36	6.96	−1844.04 (0.10)	9.35 (0.04)
$Fe_2CoIn_{0.9}Sn_{0.1}$	225	6.82	802.75	6.81	1815.55 (0.27)	6.81 (0.00)
$Rh_2MnGa_{0.8}Ge_{0.2}$	225	4.31	1012.05	6.47	2374.07 (−0.13)	−8.67 (−0.22)

[a]Theoretical results obtained with VASP, Ref. [33]
The caption is the same as in Table 1

3. Results and discussion

3.1. Identified promising chemically substituted candidates with large AHC and ANC

Figure 2 presents the absolute values of σ_{xy} and α_{xy} for 1493 candidates, categorized based on the element at the X site and represented by different symbols. The blue and red areas represent candidates that possess large $|\sigma_{xy}|$ and $|\alpha_{xy}|$, respectively, meeting criteria of $|\sigma_{xy}| = 1500$ S cm^{-1} and $|\alpha_{xy}| = 5$ A m^{-1}K^{-1}, which are determined based on the experimentally reported substantial value in Fe [57] and $SmCo_5$ [3, 58] at room temperature. From Fig. 2, it becomes evident that σ_{xy} and α_{xy} can be easily tailored by chemical substitution. Out of these candidates, 71 chemically substituted candidates (open symbols) belonging to 4 groups (Co-, Fe-, Rh- and Ru-based compounds) exceed the defined $|\sigma_{xy}|$ or $|\alpha_{xy}|$ criterion, and 3 candidates (green area) demonstrate large $|\sigma_{xy}|$ and $|\alpha_{xy}|$ simultaneously. In contrast, only 6 stoichiometric mother compounds (filled symbols) from the Rh- and Fe-based groups meet the discussed criteria. As depicted in Fig. S2 of the SM, all promising candidates mentioned above belong to the $L2_1$ type with space group number 225. It should be noted that several promising candidates (labeled in Fig. 2) originate from the same stoichiometric mother compound but with slightly

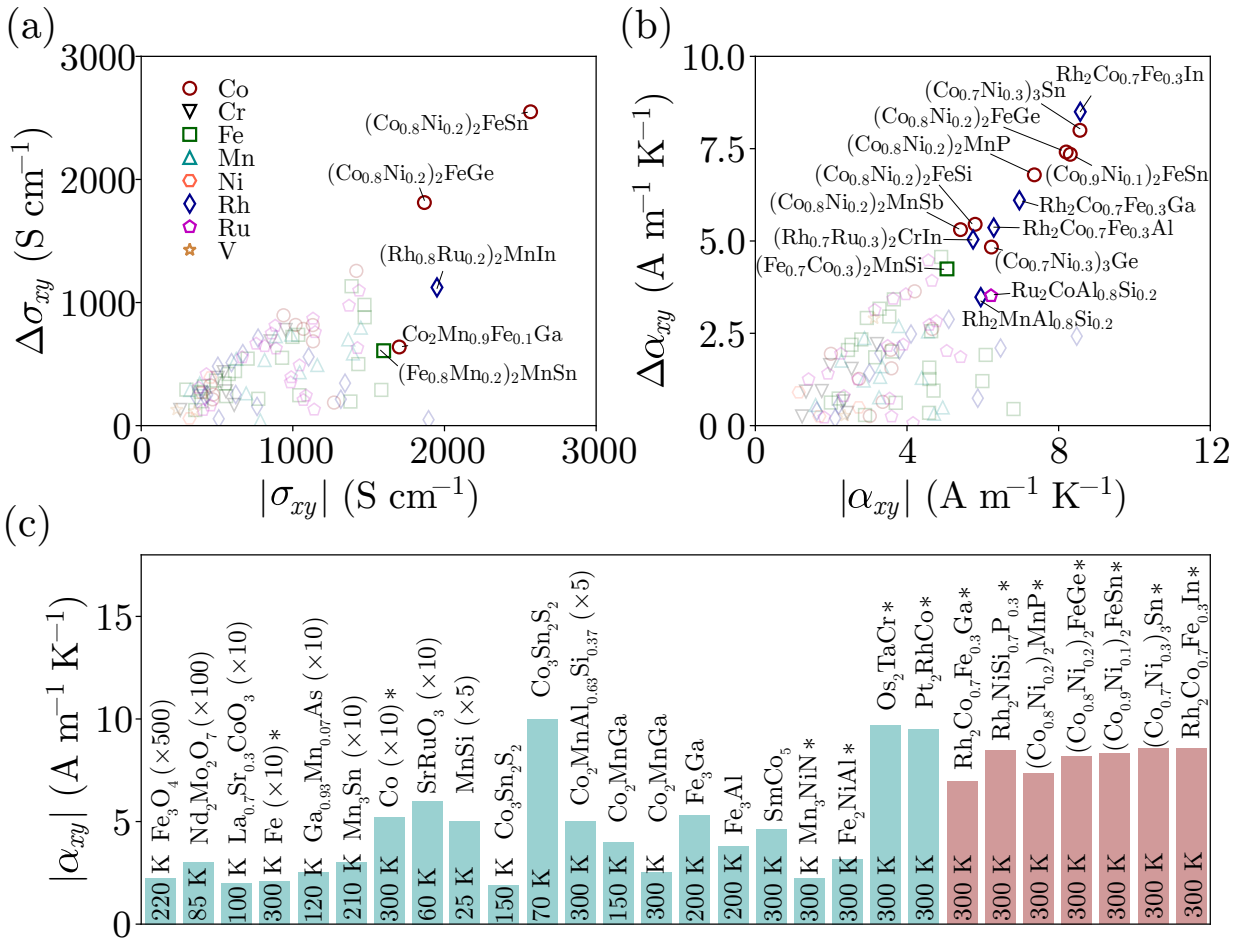

Figure 3: Enhancement of σ_{xy} (a) and α_{xy} (b) in the candidates incoparating chemical substitution in comparison with the corresponding stoichiometric mother compounds. Different symbols represent the compounds containing the same element at the X site. (c) The calculated α_{xy} for promising candidates (red color) in comparison to various magnets (cyan color) taken from previous work [8, 23, 30, 32, 57–69]. The numbers in parentheses are to scale the original data and asterisks represent the computational results.

different concentrations of substitution at different atomic sites.

To consider the wide range of potential chemically substituted materials, one candidate with the largest σ_{xy} or α_{xy} from each stoichiometric mother compound was selected, and the top 10 candidates are tabulated in Table 1 and Table 2, respectively. The complete list of materials is provided in the SM. It is evident that most chemically substituted candidates listed in Table 1 and Table 2 exhibit significantly enhanced transport quantities compared to the corresponding stoichiometric compounds, with the exception being Rh_2MnAl and Rh_2NiSn. For stoichiometric mother compounds, we obtained transport properties that are qualitatively similar to those reported by Noky *et al*. [33]. The differences can be attributed to the use of different pseudopotentials from different DFT codes. Notably, the stoichiometric compound of $Co_2Mn_{0.9}Fe_{0.1}Ga$, $(Fe_{0.8}Mn_{0.2})_2MnSn$, and $(Co_{0.8}Ni_{0.2})_2FeGe$, namely Co_2MnGa, Fe_2MnSn, and Co_2FeGe, have been already synthesized by experiments with bulk material or thin films [22, 27, 59, 69–71]. In particular, $(Co_{0.8}Ni_{0.2})_2FeGe$ exhibits simultaneously large σ_{xy} (-1867.45 S cm^{-1}) and α_{xy} (8.20 A m^{-1}K^{-1}).

We observed the largest and second largest σ_{xy} in $(Co_{0.8}Ni_{0.2})_2FeSn$ (-2568 S cm^{-1}) and $(Rh_{0.8}Ru_{0.2})_2MnIn$ (1950 S cm^{-1}), respectively. These values significantly surpass the experimentally realized values of ∼1500 S cm^{-1} in Fe [57] and rival those of Co_2MnGa, which reaches ∼2000 S cm^{-1} [59] at low temperatures. From Table 2, $Rh_2Co_{0.7}Fe_{0.3}In$ and $(Co_{0.7}Ni_{0.3})_3Sn$ exhibit the largest α_{xy} values of ∼8.6 A m^{-1}K^{-1}, followed by $Rh_2NiSi_{0.7}P_{0.3}$, $(Co_{0.9}Ni_{0.1})_2FeSn$, and $(Co_{0.8}Ni_{0.2})_2FeGe$ with α_{xy} > 8 A m^{-1}K^{-1}. These magnitudes are substantially larger than those of most typical magnets shown in Fig. 3 (c) and are comparable to the highest value reported in $Co_3Sn_2S_2$ [68] (∼10 A m^{-1}K^{-1} 70 K) and in all-*d* Heusler compounds, such as Os_2TaCr (9.7 A m^{-1}K^{-1}) and Pt_2RhCo (9.5 A m^{-1}K^{-1}), at 300 K [32]. In addition, we found that the values of σ_{xy} and α_{xy} in most chemically substituted candidates approach their maximum values (see σ_{xy}^{max} in Table 1 and α_{xy}^{max} in Table 2) within an energy window of ∼0.05 eV. This suggests that the

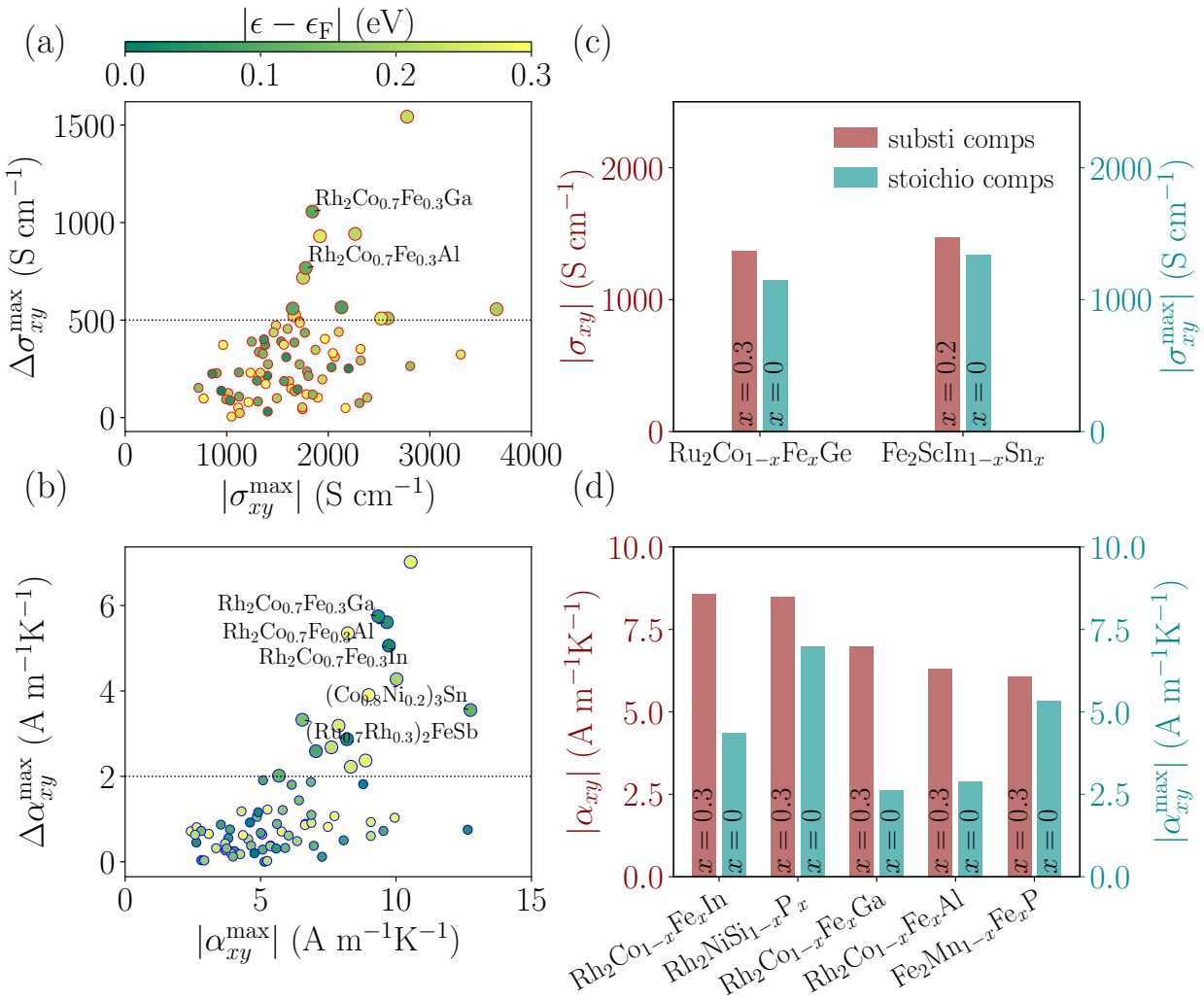

Figure 4: Enhancement of σ_{xy}^{max} (a) and α_{xy}^{max} (b) in chemically substituted candidates in comparison with the corresponding stoichiometric mother compounds. The color bar shows the energy difference of the σ_{xy}^{max} and α_{xy}^{max} with respect to the Fermi energy. Promising chemically substituted candidates (red bars) are identified where their σ_{xy} (c) and α_{xy} (d) at the Fermi energy are larger than the corresponding σ_{xy}^{max} and α_{xy}^{max} in stoichiometric mother compounds (cyan bars) within the energy range of $[-0.3:0.3]$ eV around the Fermi energy.

chemical substitution with a concentration of up to 0.3 can effectively fine-tune and optimize the transport properties of these compounds.

To quantify the efficiency of chemical substitution, we define an enhancement as $\Delta T_{xy} = T_{xy}^{\text{substi}} - T_{xy}^{\text{stoichio}}$, where T_{xy}^{substi} and T_{xy}^{stoichio} are the absolute value σ_{xy} or α_{xy} obtained from the chemically substituted candidate and the corresponding stoichiometric compound, respectively. In Fig. 3, candidates are displayed with $\Delta\sigma_{xy} \geq 500$ S cm^{-1} and $|\sigma_{xy}| \geq 1500$ S cm^{-1} [Fig. 3(a)], and with $\Delta\alpha_{xy} \geq 3$ A m^{-1}K^{-1} and $|\alpha_{xy}| \geq 5$ A m^{-1}K^{-1} [Fig. 3(b)]. For σ_{xy}, we have identified 5 candidates shown in Fig. 3(a) that meet the defined criteria. In contrast, Fig. 3(b) reveals an extensive list of 14 candidates with enhanced α_{xy} values, surpassing the defined criteria. This observation underscores the effective optimization of α_{xy} through chemical substitution. The observed phenomenon is reasonable and can be explained by the entropy density function $s(\epsilon)$ shown in Eq. (4) in the integration of BC within the FBZ. At finite temperatures, the entropy density function exhibits nonzero values within an energy window of $|\epsilon - \mu| \lesssim k_B T$. Within this window, both the occupied and unoccupied bands near the Fermi energy significantly contribute to the BC. As a result, the BC originating from these bands near the Fermi energy makes α_{xy} amenable to tailoring via chemical substitution.

In the following, we discuss the possible scenarios that explain the enhancement of σ_{xy} and α_{xy} through chemical substitution. Initially, the position of the Fermi energy ϵ_F can be easily tuned through chemical substitution, which introduces carrier (electron or hole), optimizing the transport quantities without changing the electronic structure. This straightforward concept aligns with the conventional band-filling approach, which has been widely used for estimating chemical substitution effects. In the band-filling approach,

the concentration of the substitution is estimated by the shift of ϵ_F within a rigid band structure of the stoichiometric compound. The ϵ_F in the chemically substituted candidates is determined by integrating the density of states up to the energy level equivalent to the number of valence electrons in the system.

However, it is essential to emphasize that the applicability of the band-filling approach is limited to specific compounds. As an illustration, let us consider three cases where Ni substitutes Co in Co_2MnGa and Co_2FeSn, and Fe substitutes Co in Rh_2CoIn. We observed a remarkably similar trend in the energy-dependent σ_{xy} for $(Co_{0.9}Ni_{0.1})_2MnGa$ shown in Fig. S3(a) of the SM, when employing both the VCA and band-filling approaches. The calculated values of 734.67 and 765.04 $S\,cm^{-1}$ obtained from VCA and band-filling approach, respectively, indicate the similarity of both approaches for Co_2MnGa. However, a notable discrepancy arises when evaluating the σ_{xy} of $(Co_{0.9}Ni_{0.1})_2FeSn$ [refer to Fig. S3(b)].In this case, the results obtained through VCA and band filling deviate considerably, yielding σ_{xy} values of -158.04 and -51.62 $S\,cm^{-1}$, respectively.

This discrepancy is further emphasized in the case of $Rh_2Co_{0.7}Fe_{0.3}In$. The energy-dependent σ_{xy} curves diverge dramatically between the two methods, with the band-filling approach yielding σ_{xy} value of 112.58 $S\,cm^{-1}$ and the VCA approach showing 394.57 $S\,cm^{-1}$ at the Fermi energy, as illustrated in Fig. S3(c). This discrepancy can be attributed to substantial changes in the electronic structure brought by chemical substitution. Such cases, particularly where extensive changes in the electronic structure occur, necessitate the use of VCA, as illustrated in Fig. S3(b) and (c), where band filling is inadequate. To assess the applicability of the band-filling approach, we examined the relationship between the total number of electrons at X and Y sites, denoted as N_v^{XY}, and the transport quantities. Our findings suggest that the band-filling approach may not be suitable for most candidates with substitution at the X or Y site, especially for those with $N_v^{XY} \sim 26.5$. Furthermore, the significant σ_{xy} values for $(Co_{0.8}Ni_{0.2})FeZ$ (Z = Sn, Ge) predicted by the VCA (refer to Table 1) at $N_v^{XY} = 26.4$ are unattainable via the band-filling approach. This discrepancy further underscores the importance of accurately calculating anomalous transport quantities using the VCA approach. Additionally, we observed that predicting α_{xy} using the band-filling approach is less reliable than predicting σ_{xy}. For further details, please refer to the SM.

The change in the electronic structure plays a central role in the significant enhancement of σ_{xy} and α_{xy} observed in this study. The change can be effectively quantified by analyzing the difference in the maximum transport quantities, denoted as $\Delta T_{xy}^{max} = T_{substi}^{max} - T_{stoichio}^{max}$, between the chemically substituted candidates and their respective stoichiometric compounds. Here, T_{substi}^{max} ($T_{stoichio}^{max}$) represents the maximum absolute value of either σ_{xy} or α_{xy} within an energy range of $[-0.3:0.3]$ eV around the ϵ_F for the chemically substituted (stoichiometric) compounds. A positive ΔT_{xy}^{max} denotes the noteworthy enhancement in the maximum transport quantities for chemically substituted candidates compared to their corresponding stoichiometric counterparts. This enhancement stems from the distinct distribution of BC in the FBZ, which, in turn, is influenced by the altered electronic structure.

As illustrated in Fig. 4(a) and (b), among the 104 candidates, 79 and 78 exhibited a positive value of $\Delta\sigma_{xy}^{max}$ and $\Delta\alpha_{xy}^{max}$, respectively. This observation highlights the importance of going beyond the band-filling approach to thoroughly understand the effect of chemical substitution. Additionally, Fig. 4(a) and (b) display the composition of the candidates, focusing on those with $\Delta\sigma_{xy}^{max} \geq 600$ $S\,cm^{-1}$ and $\Delta\alpha_{xy}^{max} \geq 3$ $A\,m^{-1}K^{-1}$ within an energy window of 0.15 eV around ϵ_F.

Of particular interest, this study identified a number of promising candidates in which the values of σ_{xy} (α_{xy}) for the candidates incorporating chemical substitution [indicated by red bars in Fig. 4(c) and (d)] at the Fermi energy exceeded the corresponding σ_{xy}^{max} (α_{xy}^{max}) values of their stoichiometric mother compounds [depicted by cyan bars in Fig. 4(c) and (d)] within the energy range of $[-0.3:0.3]$ eV surrounding the Fermi energy. Notably, for instance, in the case of 0.3 Fe-substituted Rh_2CoZ (Z = Al, Ga, and In) shown in Fig. 4(d), the $|\alpha_{xy}|$ values were found to be twice as large as the $|\alpha_{xy}^{max}|$ in the stoichiometric mother compounds. This discrepancy implies a substantial alteration in the band structure upon Fe-substituted Rh_2CoZ, resulting in a dramatic enhancement of BC.

3.2. Significant change of electronic structure through chemical substitution

In this section, we provide a detailed discussion of three highly promising candidates that belong to different groups of X elements, each exhibiting substantial α_{xy} values. These candidates are $Rh_2Co_{0.7}Fe_{0.3}In$, $Fe_2Mn_{0.7}Fe_{0.3}P$, and $(Co_{0.7}Ni_{0.3})_3Sn$. All of these candidates share the $L2_1$-type crystal structure [72], hosting three mirror planes at $x = 0$, $y = 0$, and $z = 0$. Previous studies [24, 33, 73] have reported the presence of three symmetry-protected nodal lines (NL) were observed at $k_x = 0$, $k_y = 0$, and $k_z = 0$ planes without including the SOC. Among these, the NL at $k_z = 0$ plane remains protected, while others at $k_x = 0$ and $k_y = 0$ planes become gapped when SOC is introduced, aligning the magnetization direction along [001] direction. The small band gap surrounding the former NL induces a strong BC. Consequently, the significant σ_{xy} or α_{xy} values are observed when the energy of the gapped NL is distributed around ϵ_F.

In addition to the previously discussed NLs, we have identified more complex NL networks near ϵ_F resulting from chemical substitution. Specifically, in the case of $Rh_2Co_{0.7}Fe_{0.3}In$, the complex NL induced by chemical substitution results in an almost twofold increase in the α_{xy} (8.57 $A\,m^{-1}K^{-1}$) at the Fermi energy when compared to the peak value (4.36 $A\,m^{-1}K^{-1}$) of the stoichiometric compound Rh_2CoIn.

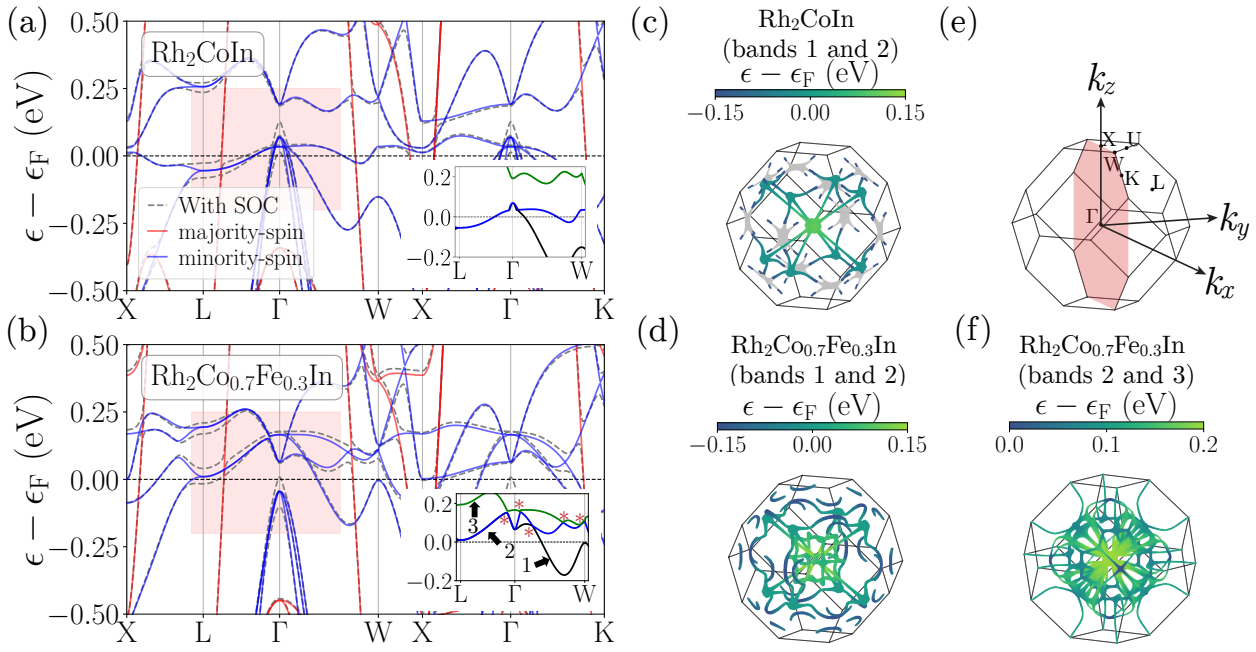

Figure 5: Band structure of Rh_2CoIn (a) and $Rh_2Co_{0.7}Fe_{0.3}In$ (b), respectively. The red and blue curves represent the majority- and minority-spin bands, respectively. Dashed gray cures are the bands computed with SOC. The inset shows the minority-spin bands in the shaded area that form nodal line networks. Asterisks show the position of the band crossing point in the nodal line. Nodal line network of Rh_2CoIn formed by bands 1 and 2 (c), and $Rh_2Co_{0.7}Fe_{0.3}In$ formed by bands 1 and 2 (d) and bands 2 and 3 (f). The color bar represents the nodal line energy window around the Fermi energy, with energies outside this window shown in gray. Note that bands 2 and 3 in Rh_2CoIn are gapped out. (e) The first Brillouin with high symmetry points and the $k_y = 0$ plane are shown with the shaded area.

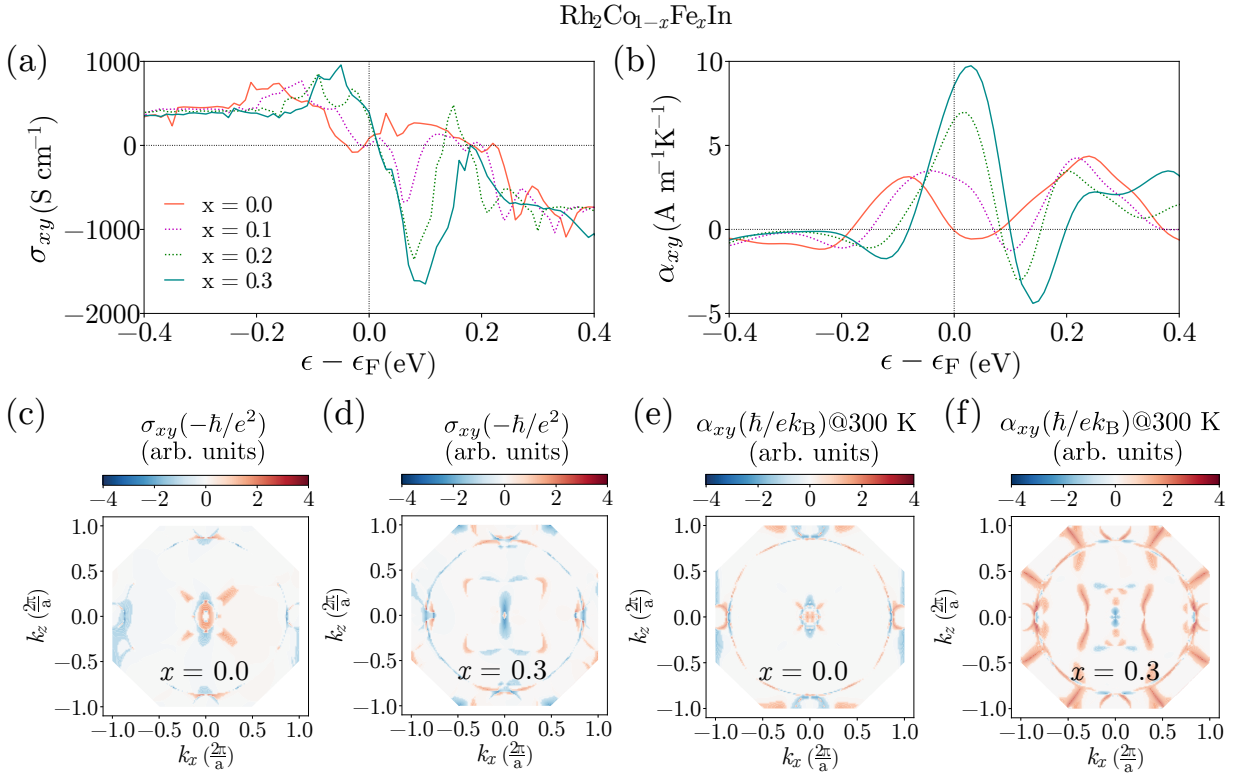

Figure 6: Energy-dependent σ_{xy} (a) and α_{xy} (b) of $Rh_2Co_{1-x}Fe_xIn$ with $x = 0, 0.1, 0.2, 0.3$, respectively. $\boldsymbol{k}$-decomposed σ_{xy} (c) and (d) and α_{xy} (e) and (f) at $k_y = 0$ plane for $Rh_2Co_{1-x}Fe_xIn$ with $x = 0$ and $x = 0.3$, respectively. Note that the color scale for σ_{xy} and α_{xy} is the same.

3.2.1. *Nodal line network creation in Rh_2CoIn through chemical substitution*

Before delving into the discussion of the band structures, we direct our attention to the magnetic moment of both the chemically substituted and stoichiometric compounds of Rh_2CoIn. Within Rh_2CoIn, the computed total magnetic moment amounts to 3.02 μ_B per formula unit (f.u.), accompanied by local moments of 2.08 and 0.52 μ_B at the corresponding Co and Rh sites, respectively. Our total magnetic moment is in good agreement with that calculated by Noky *et al*. (3.0 μ_B/f.u.) [33], alongside local moments of 2.02 and 0.52 μ_B at the Co and Rh sites, respectively. The total moment increases to 3.43 μ_B/f.u. with 0.3 Fe substituting to the Co site, primarily resulting from the enhanced local moment of 2.48 μ_B at pseudo atom Co/Fe site.

Figure 5 (a) and (b) illustrate the band structure of Rh_2CoIn and $Rh_2Co_{0.7}Fe_{0.3}In$, respectively, where the solid curves represent the majority (red) and minority (blue) spin-polarized bands, while the dashed gray curves depict the bands computed with SOC. Notably, a distinct contrast in the minority-spin bands between the chemically substituted candidates and the stoichiometric mother compounds is evident within the shaded area of Fig. 5(a) and (b), highlighting the following significant changes. First, in Rh_2CoIn, the two minority bands [as shown by the black and blue bands in the inset of Fig. 5(a)] crossing ϵ_F are shifted upwards upon Fe substitution. This is a reasonable consequence of ϵ_F shifting to lower energy due to introducing hole carrier. However, in $Rh_2Co_{0.7}Fe_{0.3}In$, the corresponding bands, labeled as 1 and 2 in the inset of Fig. 5(b), undergo dramatic modifications, forming a band crossing point along the Γ–W high-symmetry path. Second, bands 2 and 3 in $Rh_2Co_{0.7}Fe_{0.3}In$, as depicted in the inset of Fig. 5(b) intersect and give rise to several band crossing points along the L–Γ–W high-symmetry path. It is worth noting that bands 2 and 3 in the stoichiometric mother compound exhibit a gap [see the inset of Fig. 5(a)].

The NL networks formed by the bands 1 and 2 for Rh_2CoIn and $Rh_2Co_{0.7}Fe_{0.3}In$ are visualized in Fig. 5(c) and (d), respectively, with the energy difference from ϵ_F indicated by the color bar. The NL networks are analyzed without considering the SOC to understand the topological properties. The degeneracy along Γ–L in the NL network is observed for both cases. However, a distinct feature emerges in the case with chemical substitution where three nodal loops are formed at $k_x = 0, k_y = 0$, and $k_z = 0$ mirror planes. Intriguingly, a more complex NL network, formed by bands 2 and 3 is exclusively identified in the chemically substituted candidate, as shown in Fig. 5(f). The NL network's energy resides above the Fermi energy within a range of 0.2 eV, suggesting its contribution solely to α_{xy}, as further elaborated below.

Next, we discuss the underlying factors behind the notable α_{xy} observed in $Rh_2Co_{0.7}Fe_{0.3}In$. To comprehensively understand the relationship between σ_{xy} and α_{xy}, α_{xy} can be formulated as,

$$\alpha_{xy} = -\frac{k_B}{e}\int d\epsilon s(\epsilon)\frac{\partial\sigma_{xy}(\epsilon, T=0)}{\partial\epsilon}. \quad (6)$$

As Eq. (6) illustrates, the magnitude of α_{xy} is directly proportional to the energy derivative of σ_{xy} weighted by the entropy density function $s(\epsilon)$. Given $s(\epsilon)$ is like a smeared delta function around ϵ_F [69], α_{xy} can be roughly estimated from $\partial\sigma_{xy}/\partial\epsilon$ around $\epsilon = \epsilon_F$.

Figure 6 (a) and (b) present the energy dependence of σ_{xy} and α_{xy} within $Rh_2Co_{1-x}Fe_xIn$, with x ranging from 0.0 to 0.3 in increments of 0.1. In Fig. 6(a), a distinct feature of Fe substitution is observed: the peak value of Rh_2CoIn, initially near ∼−0.2 eV, gradually shifts to higher energy with increasing x. This shift is accompanied by the emergence of a negative slope around the Fermi energy as x increases. Eventually, in $Rh_2Co_{0.7}Fe_{0.3}In$, a substantial peak value of -1649.50 S cm^{-1} is achieved at 0.1 eV above the Fermi energy. In contrast, the stoichiometric mother compound lacks this negative peak. The consequential negative energy-dependent slope in σ_{xy} leads to a giant α_{xy} of 8.57 A m^{-1}K^{-1} at 300 K shown in Fig. 6(b).

We investigated the $\boldsymbol{k}$-decomposed σ_{xy} and α_{xy} at $k_y = 0$ plane, where the NL becomes gapped in the presence of SOC. This analysis provides deeper insights into the substantial α_{xy} observed in $Rh_2Co_{0.7}Fe_{0.3}In$. When examining the σ_{xy} for both compounds in Fig. 6(c) and (d) and α_{xy} for Rh_2CoIn in Fig. 6(e), a distinct lack of large values in the plane becomes evident. In contrast, Fig. 6(f) reveals a noticeable positive $\boldsymbol{k}$-decomposed pattern with significant α_{xy} values for $Rh_2Co_{0.7}Fe_{0.3}In$. This pattern is consistent with the NL loops around Γ and W points [see the position in Fig. 5(e)], originating from the gapped NL networks shown in Fig. 5 (d) and (f) exclusively to the chemically substituted materials. It is worth noting that the energy of the mentioned NL networks is mainly located above ϵ_F, rendering them irrelevant to the contribution of σ_{xy}.

3.2.2. *Nodal line network modification through chemical substitution*

The creation of NL networks through chemical substitution, as observed in the $Rh_2Co_{1-x}Fe_xIn$, is not a common occurrence. In most general cases, the Fermi energy can be effectively tuned via chemical substitution. Simultaneously, the band structure undergoes slight modifications due to chemical substitution, impacting the energy-dependent behavior of BC and subsequently leading to alterations in the transport quantities. Here, we take the $Fe_2Mn_{0.7}Fe_{0.3}P$ and $(Co_{0.7}Ni_{0.3})_3Sn$ as examples, to illustrate the enhancement of α_{xy} through the shift of the Fermi energy accompanied by the band structure modifications via chemical substitution.

The ferromagnetic state was observed in Fe_2MnP, where the total magnetic moment is 3.97 μ_B/f.u., with local moments of 2.55 and 0.69 μ_B at Mn and Fe sites, respectively. The observed moments are consistent with reported values (μ_{tot} = 4 μ_B/f.u., μ_{Mn} = 2.6 μ_B, μ_{Fe} = 0.7 μ_B, Ref. [24]). A total moment of 4.30 μ_B/f.u. was

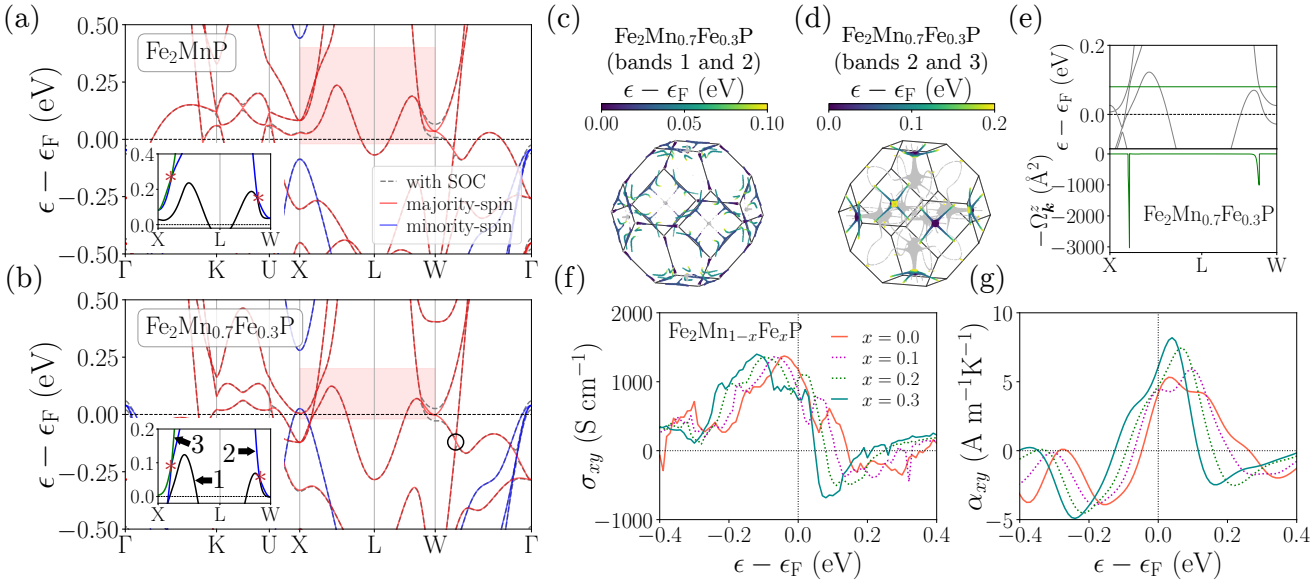

Figure 7: Band structure of Fe_2MnP (a) and $Fe_2Mn_{0.7}Fe_{0.3}P$ (b), respectively. The red and blue curves represent the majority- and minority-spin bands, respectively. Dashed gray cures are the bands computed with SOC. The inset shows the majority-spin bands in the shaded area that form nodal line networks. Asterisks show the position of the band crossing point in the nodal line. Nodal line network of $Fe_2Mn_{0.7}Fe_{0.3}P$ formed by bands 1 and 2 (c), and bands 2 and 3 (d), respectively. The color bar represents the nodal line energy window around the Fermi energy, with energies outside this window shown in gray. (e) Berry curvature $\Omega_{\boldsymbol{k}}^{z}$ evaluated at 0.08 eV (green line) above the Fermi energy along the high-symmetry path. Energy-dependent σ_{xy} (f) and α_{xy} (g) for $Fe_2Mn_{1-x}Fe_xP$ with $x = 0$, 0.1, 0.2, 0.3, respectively.

obtained for $Fe_2Mn_{0.7}Fe_{0.3}P$, with an increase of ∼0.1 μ_B at each Mn/Fe and Fe site. In contrast, the total moment of 4.16 μ_B/f.u. (4.04 μ_B in Ref. [33]) in Co_3Sn, which decreases to 3.15 μ_B/f.u. when 0.3 Ni was substituted at the Co site.

The band structures of Fe_2MnP and $Fe_2Mn_{0.7}Fe_{0.3}P$ are presented in Fig. 7 (a), and (b), respectively. It is evident that the overall band structures for these two cases exhibit notable similarities, with only minor modifications such as the location of ϵ_F and the band dispersion along specific high-symmetry paths. Interestingly, these subtle adjustments lead to the enhancement of α_{xy} in the chemically substituted candidates, a point we will elaborate upon. In both compounds, the intriguing topological properties stem from the majority-spin bands, highlighted in the shaded areas of Fig. 7(a) and (b), respectively. Given the similarity of NL networks in both chemically substituted and mother compounds, here we focus on the $Fe_2Mn_{0.7}Fe_{0.3}P$ compound.

We have identified three distinct types of NL networks near the Fermi energy. The first, formed by two majority bands [indicated by the black circle in Fig. 7(b)], is shown in Fig. S5 of the SM. The NL networks are located at the three mirror planes of $k_x = 0$, $k_y = 0$, and $k_z = 0$, respectively, with their energies mainly distributed below the Fermi energy. This specific NL has been extensively discussed by Noky *et al.* [24] and serves as the main reason for the large σ_{xy} for both compounds. As depicted in Fig. 7(f), the $\sigma_{xy}^{\max}$, with the values of ∼1400 S cm^{-1} for both compounds mainly originates from the BC induced by this gapped NL.

The second and third NL networks, depicted in Fig. 7(c) and (d), are formed by bands 1 and 2, and bands 2 and 3 [refer to the inset of Fig. 7(b)], respectively. These NL networks are less commonly discussed, primarily due to their NL energies predominantly residing mainly above ϵ_F, which makes a minor contribution to σ_{xy}. Nevertheless, we observed subtle changes in the band dispersion of these bands upon chemical substitution. However, a discernible difference appears in the energy of the band crossing points along X–L–W high-symmetry path between the chemically substituted and stoichiometric compounds. This energy difference is pivotal in explaining the significant α_{xy} observed in $Fe_2Mn_{0.7}Fe_{0.3}P$.

In Fe_2MnP, the two band crossing points shown in the inset of Fig. 7(a), formed by bands 1 and 2, and bands 2 and 3, are situated considerably away from ϵ_F, at 0.17 and 0.3 eV above ϵ_F, respectively. Through substituting Fe at the Mn site, both band crossing points shown in the inset of Fig. 7(b) shift towards the Fermi energy. Importantly, these two points nearly converge to an energy level of $\epsilon - \epsilon_F$∼0.08 eV. As a consequence, two significant BCs are simultaneously induced at 0.08 eV above ϵ_F along the X–L–W high-symmetry path by the aforementioned points in the presence of SOC, as demonstrated in Fig. 7(e). These substantial BCs result in a steep negative slope in the energy-dependent σ_{xy} within 0.08 eV above ϵ_F, as depicted in Fig. 7(f). This slope gives rise to a considerable α_{xy} value of 6.08 A m^{-1}K^{-1} at ϵ_F in $Fe_2Mn_{0.7}Fe_{0.3}P$, as illustrated in Fig. 7(g).

Importantly, it is worth noting that this α_{xy} is not the peak, as the maximum value of 8.19 A m^{-1}K^{-1} is found

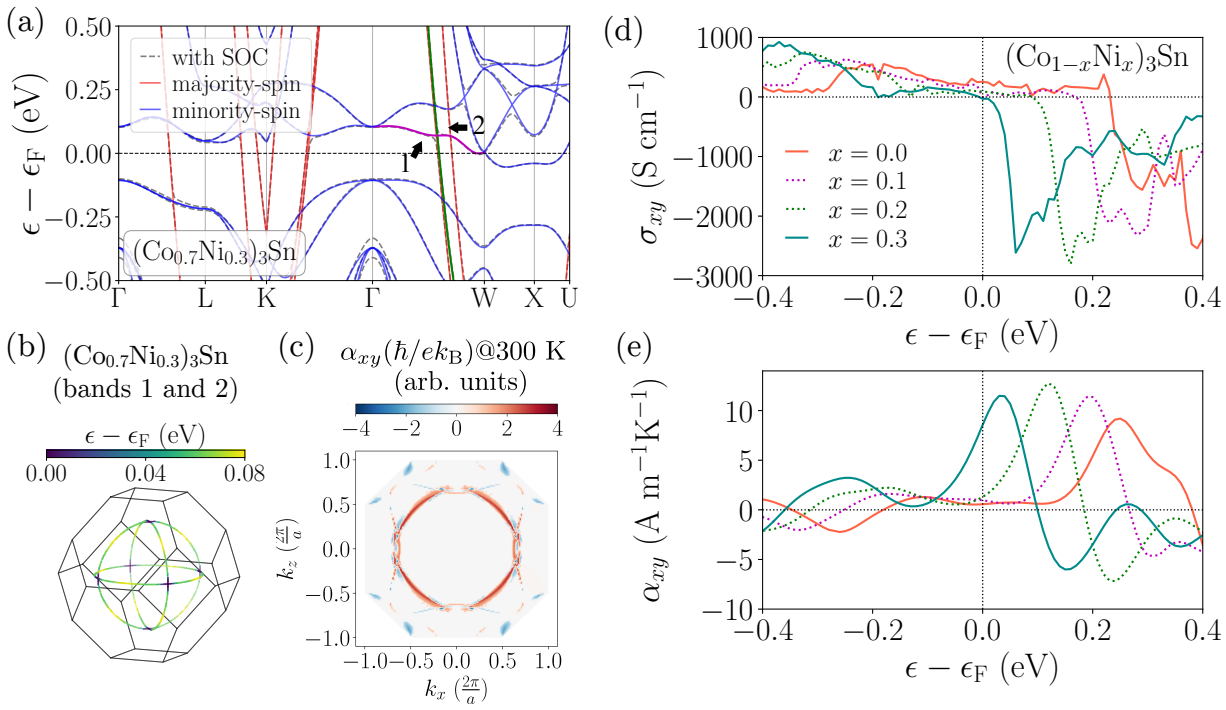

Figure 8: (a) Band structure of $(Co_{0.7}Ni_{0.3})_3Sn$. The red and blue curves represent the majority- and minority-spin bands, respectively. Dashed gray cures are the bands computed with SOC. The minority-spin band labeled 1 and the majority-spin band labeled 2 formed the nodal line. (b) Nodal line network of $(Co_{0.7}Ni_{0.3})_3Sn$ formed by bands 1 and 2. The color bar represents the nodal line energy window around the Fermi energy. (c) $\boldsymbol{k}$-decomposed α_{xy} of at $k_y = 0$ plane for $(Co_{0.7}Ni_{0.3})_3Sn$. Energy-dependent σ_{xy} (d) and α_{xy} (e) of $(Co_{1-x}Ni_x)_3Sn$ with $x = 0$, 0.1, 0.2, 0.3, respectively.

merely 0.04 eV above ϵ_F. In contrast, even the α_{xy}^{max} in the stoichiometric compound is 5.32 A m^{-1}K^{-1} [at 0.03 eV above ϵ_F in Fig. 7(g)], highlighting the significant impact of minor NL network modifications stemming from chemical substitution, which subsequently induce considerable α_{xy} values. For further details on the relatively modest α_{xy} in Fe_2MnP, please refer to the SM.

Finally, Ni-substituted Co_3Sn is discussed. Our analysis reveals that the bands forming the NL network arise from the different spin states. We note that the NL formed by different spin states occupies a narrow energy range. Through chemical substitution, we strategically shift the Fermi energy to align with the NL energy, consequently resulting in the generation of substantial σ_{xy} and α_{xy} values. Intriguingly, we observed the common feature in $(Co_{1-x}Ni_x)_2FeSn$ [refer to the energy-dependent anomalous transport properties in Fig. S7 of the SM], and among various Ni-substituted Co_2XZ systems (Y = Co, Fe; Z = Sn, Ge) with substantial σ_{xy} or α_{xy} values shown in Fig. 2. Illustrating this with $(Co_{0.7}Ni_{0.3})_3Sn$, we observed in Fig. 8 (a) the intersection of minority- and majority-spin bands, labeled as 1 and 2 respectively, along the Γ–W high-symmetry path. These intersecting bands give rise to three NLs, as depicted in Fig. 8(b), situated at the previously mentioned mirror planes. It is important to note that the energy of these NLs resides above ϵ_F, encompassed within a narrow energy window of 0.08 eV.

The presence of a robust BC becomes apparent within this energy window, originating from the gapped NLs with SOC. Consequently, we observe a distinct negative peak value of −2614.20 S cm^{-1} in σ_{xy} for $(Co_{0.7}Ni_{0.3})_3Sn$, located 0.06 eV above ϵ_F, as evident in Fig. 8(d). A remarkable α_{xy} of 8.56 A m^{-1}K^{-1} [see Fig. 8(e)] was obtained, with clear $\boldsymbol{k}$-decomposed α_{xy} distributed along the gapped NLs, as illustrated in Fig. 8(c). Worth mentioning is the energy in the corresponding NLs of the stoichiometric mother compounds, located ∼0.3 eV above ϵ_F, resulting in a negligible contribution to both σ_{xy} and α_{xy}.

4. Summary

In summary, our study involves an extensive high-throughput calculation of 1493 magnetic cubic Heusler compounds, incorporating chemical substitution through first-principles calculations, aimed at identifying promising candidates with enhanced transport properties. These candidates are categorized based on the element at the X site. Notably, compounds based on Co and Rh demonstrate remarkable potential for optimization of the transport property. Specifically, the compound $(Co_{0.8}Ni_{0.2})_2FeSn$ exhibits exceptional perfomance, with both giant σ_{xy} and α_{xy} (T = 300 K) values of −2567 S cm^{-1} and 8.27 A m^{-1}K^{-1}, respectively. These values surpass both experimental and theoretical results reported for other typical magnets [32, 33, 57, 74].

Additionally, we highlight that 5 candidates derived from distinct stoichiometric mother compounds exhibit α_{xy} values exceeding 8 $\mathrm{A\,m^{-1}K^{-1}}$. The magnitude of these values is comparable to those reported for $Co_3Sn_2S_2$ [68] and several recently explored all-d Heusler compounds [32].

Furthermore, we emphasize the pivotal role of evaluating the chemical substition effects using VCA, as opposed to relying solely on the band-filling approach with stoichiometric mother compounds. The approach we employed not only takes into account the shift in Fermi energy but also counts the significant modification in the band structure through chemical substitution. As a result, we have identified a number of promising candidates, especially in the case of $Rh_2Co_{0.7}Fe_{0.3}Z$ (Z = Al, Ga, In), where the α_{xy} exceed the maximum observed in the stoichiometric mother compounds. Through a detailed analysis of the band structure, we revealed that the creation or modification of nodal lines via chemical substitution leads to a strong BC slightly above the Fermi energy and consequently yields substantial α_{xy}. Our work provides valuable insights into the optimization of transport properties by chemical substitution, thereby paving the way for the search for new high-performance Heusler compounds.

Declaration of Competing Interest

The authors declare that they have no known competing financial interests or personal relationships that could have appeared to influence the work reported in this paper.

Acknowledgments

We thank Dr. E. Xiao, Dr. W. Zhou, Dr. Y. Sakuraba and Dr. Y. Iwasaki at the National Institute for Materials Science (NIMS) for fruitful discussion. This work was supported by JST-CREST Grant Number JPMJCR21O1 and by MEXT Program: Data Creation and Utilization-Type Material Research and Development Project (Digital Transformation Initiative Center for Magnetic Materials) Grant Number JPMXP1122715503 and by JST-ERATO Grant Number JPMJER2201. The calculations in this study were performed on the Numerical Materials Simulator at NIMS.

References

[1] T. J. Seebeck, Ueber die magnetische polarisation der metalle und erze durch temperaturdifferenz, Ann. Phys. 82 (3) (1826) 253–286. doi:10.1002/andp.18260820302.

[2] K.-i. Uchida, Anisotropy boosts transverse thermoelectrics, Nat. Mater. 21 (2) (2022) 136–137. doi:10.1038/s41563-021-01160-7.

[3] K.-i. Uchida, W. Zhou, Y. Sakuraba, Transverse thermoelectric generation using magnetic materials, Appl. Phys. Lett. 118 (14) (2021) 140504. doi:10.1063/5.0046877.

[4] M. Mizuguchi, S. Nakatsuji, Energy-harvesting materials based on the anomalous nernst effect, Sci. Technol. Adv. Mater. 20 (1) (2019) 262–275. doi:10.1080/14686996.2019.1585143.

[5] N. Nagaosa, J. Sinova, S. Onoda, A. H. MacDonald, N. P. Ong, Anomalous Hall effect, Rev. Mod. Phys. 82 (2010) 1539–1592. doi:10.1103/RevModPhys.82.1539.

[6] D. Xiao, J. Shi, Q. Niu, Berry phase correction to electron density of states in solids, Phys. Rev. Lett. 95 (2005) 137204. doi:10.1103/PhysRevLett.95.137204.

[7] Y. Yao, L. Kleinman, A. H. MacDonald, J. Sinova, T. Jungwirth, D.-s. Wang, E. Wang, Q. Niu, First principles calculation of anomalous Hall conductivity in ferromagnetic bcc Fe, Phys. Rev. Lett. 92 (2004) 037204. doi:10.1103/PhysRevLett.92.037204.

[8] A. Sakai, S. Minami, T. Koretsune, T. Chen, T. Higo, Y. Wang, T. Nomoto, M. Hirayama, S. Miwa, D. Nishio-Hamane, F. Ishii, R. Arita, S. Nakatsuji, Iron-based binary ferromagnets for transverse thermoelectric conversion, Nature 581 (7806) (2020) 53–57. doi:10.1038/s41586-020-2230-z.

[9] Y. Pan, C. Le, B. He, S. J. Watzman, M. Yao, J. Gooth, J. P. Heremans, Y. Sun, C. Felser, Giant anomalous Nernst signal in the antiferromagnet $YbMnBi_2$, Nat. Mater. 21 (2) (2022) 203–209. doi:10.1038/s41563-021-01149-2.

[10] D. F. Liu, A. J. Liang, E. K. Liu, Q. N. Xu, Y. W. Li, C. Chen, D. Pei, W. J. Shi, S. K. Mo, P. Dudin, T. Kim, C. Cacho, G. Li, Y. Sun, L. X. Yang, Z. K. Liu, S. S. P. Parkin, C. Felser, Y. L. Chen, Magnetic Weyl semimetal phase in a Kagomé crystal, Science 365 (6459) (2019) 1282–1285. doi:10.1126/science.aav2873.

[11] T. Chen, T. Tomita, S. Minami, M. Fu, T. Koretsune, M. Kitatani, I. Muhammad, D. Nishio-Hamane, R. Ishii, F. Ishii, R. Arita, S. Nakatsuji, Anomalous transport due to Weyl fermions in the chiral antiferromagnets Mn_3X, X = Sn, Ge, Nat. Commun. 12 (1) (2021) 572. doi:10.1038/s41467-020-20838-1.

[12] K. Kim, J. Seo, E. Lee, K.-T. Ko, B. S. Kim, B. G. Jang, J. M. Ok, J. Lee, Y. J. Jo, W. Kang, J. H. Shim, C. Kim, H. W. Yeom, B. I. Min, B.-J. Yang, J. S. Kim, Large anomalous Hall current induced by topological nodal lines in a ferromagnetic van der waals semimetal, Nat. Mater. 17 (9) (2018) 794–799. doi:10.1038/s41563-018-0132-3.

[13] T. Suzuki, R. Chisnell, A. Devarakonda, Y.-T. Liu, W. Feng, D. Xiao, J. W. Lynn, J. G. Checkelsky, Large anomalous Hall effect in a half-Heusler antiferromagnet, Nat. Phys. 12 (12) (2016) 1119–1123. doi:10.1038/nphys3831.

[14] Y. He, S. Schneider, T. Helm, J. Gayles, D. Wolf, I. Soldatov, H. Borrmann, W. Schnelle, R. Schaefer, G. H. Fecher, B. Rellinghaus, C. Felser, Topological Hall effect arising from the mesoscopic and microscopic non-coplanar magnetic structure in MnBi, Acta Mater. 226 (2022) 117619. doi:10.1016/j.actamat.2022.117619.

[15] C. Fu, Y. Sun, C. Felser, Topological thermoelectrics, APL Mater. 8 (4) (2020). doi:10.1063/5.0005481.

[16] I. Kurniawan, K. Nawa, K. Masuda, Y. Miura, K. Hono, First-principles disordered local-moment study on temperature dependence of spin polarization in $Co_2Fe(Ga_{0.5}Ge_{0.5})$ Heusler alloy, Acta Mater. 218 (2021) 117218. doi:10.1016/j.actamat.2021.117218.

[17] K. Hu, R. Xie, C. Shen, H. Peng, H. Liu, H. Zhang, High-throughput design of co-based magnetic heusler compounds, Acta Mater. 259 (2023) 119255. doi:10.1016/j.actamat.2023.119255.

[18] M. Ye, A. Kimura, Y. Miura, M. Shirai, Y. T. Cui, K. Shimada, H. Namatame, M. Taniguchi, S. Ueda, K. Kobayashi, R. Kainuma, T. Shishido, K. Fukushima, T. Kanomata, Role of electronic structure in the martensitic phase transition of $Ni_2Mn_{1+x}Sn_{1-x}$ studied by hard-x-ray photoelectron spectroscopy and ab initio calculation, Phys. Rev. Lett. 104 (2010) 176401. doi:10.1103/PhysRevLett.104.176401.

[19] M. Takhsha Ghahfarokhi, F. Casoli, C. Minnert, S. Bruns, E. Bruder, R. Cabassi, K. Durst, O. Gutfleisch, F. Albertini, Effects of nanoindents on the martensitic transformation of Ni-Mn-Ga shape-memory Heusler films: A study by high-resolution imaging as a function of temperature, Acta Mater. 245 (2023) 118603. doi:10.1016/j.actamat.2022.118603.

[20] A. Taubel, B. Beckmann, L. Pfeuffer, N. Fortunato, F. Scheibel, S. Ener, T. Gottschall, K. P. Skokov, H. Zhang, O. Gutfleisch, Tailoring magnetocaloric effect in all-d-metal Ni-Co-Mn-Ti Heusler alloys: a combined experimental and theoretical study, Acta Mater. 201 (2020) 425–434. doi:10.1016/j.actamat.2020.10.013.

[21] K. Manna, L. Muechler, T.-H. Kao, R. Stinshoff, Y. Zhang, J. Gooth, N. Kumar, G. Kreiner, K. Koepernik, R. Car, J. Kübler, G. H. Fecher, C. Shekhar, Y. Sun, C. Felser, From colossal to zero: Controlling the anomalous Hall effect in magnetic Heusler compounds via Berry curvature design, Phys. Rev. X 8 (2018) 041045. doi:10.1103/PhysRevX.8.041045.

[22] K. Sumida, Y. Sakuraba, K. Masuda, T. Kono, M. Kakoki, K. Goto, W. Zhou, K. Miyamoto, Y. Miura, T. Okuda, A. Kimura, Spin-polarized Weyl cones and giant anomalous Nernst effect in ferromagnetic Heusler films, Commun. Mater. 1 (1) (2020) 89. doi:10.1038/s43246-020-00088-w.

[23] X. Yang, W. Feng, X.-P. Li, G.-B. Liu, Y. Mokrousov, Y. Yao, Intrinsic and extrinsic anomalous transport properties of the Heusler ferromagnets Fe_2CoAl and Fe_2NiAl from first principles, Phys. Rev. B 107 (2023) 224405. doi:10.1103/PhysRevB.107.224405.

[24] J. Noky, Q. Xu, C. Felser, Y. Sun, Large anomalous Hall and Nernst effects from nodal line symmetry breaking in Fe_2MnX (X = P, As, Sb), Phys. Rev. B 99 (2019) 165117. doi:10.1103/PhysRevB.99.165117.

[25] J. Noky, J. Gooth, C. Felser, Y. Sun, Characterization of topological band structures away from the fermi level by the anomalous Nernst effect, Phys. Rev. B 98 (2018) 241106. doi:10.1103/PhysRevB.98.241106.

[26] I. Belopolski, K. Manna, D. S. Sanchez, G. Chang, B. Ernst, J. Yin, S. S. Zhang, T. Cochran, N. Shumiya, H. Zheng, B. Singh, G. Bian, D. Multer, M. Litskevich, X. Zhou, S.-M. Huang, B. Wang, T.-R. Chang, S.-Y. Xu, A. Bansil, C. Felser, H. Lin, M. Z. Hasan, Discovery of topological Weyl fermion lines and drumhead surface states in a room temperature magnet, Science 365 (6459) (2019) 1278–1281. doi:10.1126/science.aav2327.

[27] S. N. Guin, K. Manna, J. Noky, S. J. Watzman, C. Fu, N. Kumar, W. Schnelle, C. Shekhar, Y. Sun, J. Gooth, C. Felser, Anomalous Nernst effect beyond the magnetization scaling relation in the ferromagnetic heusler compound Co_2MnGa, NPG Asia Mater. 11 (1) (2019) 16. doi:10.1038/s41427-019-0116-z.

[28] S. Minami, F. Ishii, M. Hirayama, T. Nomoto, T. Koretsune, R. Arita, Enhancement of the transverse thermoelectric conductivity originating from stationary points in nodal lines, Phys. Rev. B 102 (2020) 205128. doi:10.1103/PhysRevB.102.205128.

[29] J. Shen, Q. Yao, Q. Zeng, H. Sun, X. Xi, G. Wu, W. Wang, B. Shen, Q. Liu, E. Liu, Local disorder-induced elevation of intrinsic anomalous Hall conductance in an electron-doped magnetic Weyl semimetal, Phys. Rev. Lett. 125 (2020) 086602. doi:10.1103/PhysRevLett.125.086602.

[30] Y. Sakuraba, K. Hyodo, A. Sakuma, S. Mitani, Giant anomalous Nernst effect in the $Co_2MnAl_{1-x}Si_x$ Heusler alloy induced by fermi level tuning and atomic ordering, Phys. Rev. B 101 (2020) 134407. doi:10.1103/PhysRevB.101.134407.

[31] J. Hu, B. Ernst, S. Tu, M. Kuveždić, A. Hamzić, E. Tafra, M. Basletić, Y. Zhang, A. Markou, C. Felser, A. Fert, W. Zhao, J.-P. Ansermet, H. Yu, Anomalous Hall and Nernst effects in Co_2TiSn and $Co_2Ti_{0.6}V_{0.4}Sn$ Heusler thin films, Phys. Rev. Appl. 10 (2018) 044037. doi:10.1103/PhysRevApplied.10.044037.

[32] M. F. Tanzim, N. Fortunato, I. Samathrakis, R. Xie, I. Opahle, O. Gutfleisch, H. Zhang, Giant anomalous Hall and Nernst conductivities in magnetic all-d metal Heusler alloys, Adv. Funct. Mater. 33 (28) (2023) 2214967. doi:10.1002/adfm.202214967.

[33] J. Noky, Y. Zhang, J. Gooth, C. Felser, Y. Sun, Giant anomalous Hall and Nernst effect in magnetic cubic Heusler compounds, npj Comput. Mater. 6 (1) (2020) 77. doi:10.1038/s41524-020-0342-5.

[34] L. Bellaiche, D. Vanderbilt, Virtual crystal approximation revisited: Application to dielectric and piezoelectric properties of perovskites, Phys. Rev. B 61 (12) (2000) 7877. doi:10.1103/PhysRevB.61.7877.

[35] Y. Yanagi, J. Ikeda, K. Fujiwara, K. Nomura, A. Tsukazaki, M.-T. Suzuki, First-principles investigation of magnetic and transport properties in hole-doped shandite compounds $Co_3In_xSn_{2-x}S_2$, Phys. Rev. B 103 (2021) 205112. doi:10.1103/PhysRevB.103.205112.

[36] H. Zhang, S. Blügel, Y. Mokrousov, Anisotropic intrinsic anomalous Hall effect in ordered 3dPt alloys, Phys. Rev. B 84 (2011) 024401. doi:10.1103/PhysRevB.84.024401.

[37] H.-L. Huang, J.-C. Tung, G.-Y. Guo, Anomalous Hall effect and current spin polarization in Co_2FeX Heusler compounds (X = Al, Ga, In, Si, Ge, andSn): A systematic ab initio study, Phys. Rev. B 91 (2015) 134409. doi:10.1103/PhysRevB.91.134409.

[38] M. I. Aroyo, J. M. Perez-Mato, D. Orobengoa, E. Tasci, G. de la Flor, A. Kirov, Crystallography online: Bilbao crystallographic server, Bulg. Chem. Commun 43 (2) (2011) 183–197.
URL https://www.cryst.ehu.es

[39] M. I. Aroyo, J. M. Perez-Mato, C. Capillas, E. Kroumova, S. Ivantchev, G. Madariaga, A. Kirov, H. Wondratschek, Bilbao crystallographic server: I. databases and crystallographic computing programs, Z. Kristallogr. Cryst. Mater. 221 (1) (2006) 15–27. doi:10.1524/zkri.2006.221.1.15.

[40] M. I. Aroyo, A. Kirov, C. Capillas, J. Perez-Mato, H. Wondratschek, Bilbao crystallographic server. II. Representations of crystallographic point groups and space groups, Acta Crystallogr. A 62 (2) (2006) 115–128. doi:10.1107/S0108767305040286.

[41] M. Seemann, D. Ködderitzsch, S. Wimmer, H. Ebert, Symmetry-imposed shape of linear response tensors, Phys. Rev. B 92 (2015) 155138. doi:10.1103/PhysRevB.92.155138.

[42] M. Park, G. Han, S. H. Rhim, Anomalous Hall effect in a compensated ferrimagnet: Symmetry analysis for Mn_3Al, Phys. Rev. Res. 4 (2022) 013215. doi:10.1103/PhysRevResearch.4.013215.

[43] D. Xiao, M.-C. Chang, Q. Niu, Berry phase effects on electronic properties, Rev. Mod. Phys. 82 (2010) 1959–2007. doi:10.1103/RevModPhys.82.1959.

[44] M. P. Ghimire, J. I. Facio, J.-S. You, L. Ye, J. G. Checkelsky, S. Fang, E. Kaxiras, M. Richter, J. Van Den Brink, Creating Weyl nodes and controlling their energy by magnetization rotation, Phys. Rev. Res. 1 (3) (2019) 032044. doi:10.1103/PhysRevResearch.1.032044.

[45] D. Xiao, Y. Yao, Z. Fang, Q. Niu, Berry-phase effect in anomalous thermoelectric transport, Phys. Rev. Lett. 97 (2006) 026603. doi:10.1103/PhysRevLett.97.026603.

[46] P. Giannozzi, S. Baroni, N. Bonini, M. Calandra, R. Car, C. Cavazzoni, D. Ceresoli, G. L. Chiarotti, M. Cococcioni, I. Dabo, A. D. Corso, S. de Gironcoli, S. Fabris, G. Fratesi, R. Gebauer, U. Gerstmann, C. Gougoussis, A. Kokalj, M. Lazzeri, L. Martin-Samos, N. Marzari, F. Mauri, R. Mazzarello, S. Paolini, A. Pasquarello, L. Paulatto, C. Sbraccia, S. Scandolo, G. Sclauzero, A. P. Seitsonen, A. Smogunov, P. Umari, R. M. Wentzcovitch, QUANTUM ESPRESSO: a modular and open-source software project for quantum simulations of materials, J. Phys.: Condens. Matter 21 (39) (2009) 395502. doi:10.1088/0953-8984/21/39/395502.

[47] P. Giannozzi, O. Andreussi, T. Brumme, O. Bunau, M. B. Nardelli, M. Calandra, R. Car, C. Cavazzoni, D. Ceresoli, M. Cococcioni, N. Colonna, I. Carnimeo, A. D. Corso, S. de Gironcoli, P. Delugas, R. A. DiStasio, A. Ferretti, A. Floris, G. Fratesi, G. Fugallo, R. Gebauer, U. Gerstmann, F. Giustino, T. Gorni, J. Jia, M. Kawamura, H.-Y. Ko, A. Kokalj, E. Küçükbenli, M. Lazzeri, M. Marsili, N. Marzari, F. Mauri, N. L. Nguyen, H.-V. Nguyen, A. O. de-la Roza, L. Paulatto, S. Poncé, D. Rocca, R. Sabatini, B. Santra, M. Schlipf, A. P. Seitsonen, A. Smogunov, I. Timrov, T. Thonhauser, P. Umari, N. Vast, X. Wu, S. Baroni, Advanced capabilities for materials modelling with Quantum ESPRESSO, J. Phys.: Condens. Matter 29 (46) (2017) 465901. doi:10.1088/1361-648X/aa8f79.

[48] J. P. Perdew, K. Burke, M. Ernzerhof, Generalized gradient approximation made simple, Phys. Rev. Lett. 77 (1996) 3865–3868. doi:10.1103/PhysRevLett.77.3865.

[49] D. R. Hamann, Optimized norm-conserving Vanderbilt pseudopotentials, Phys. Rev. B 88 (2013) 085117, Erratum Phys. Rev. B 95, 239906 (2017). doi:10.1103/PhysRevB.88.085117.

[50] M. J. van Setten, M. Giantomassi, E. Bousquet, M. J. Verstraete, D. R. Hamann, X. Gonze, G.-M. Rignanese, The pseudodojo: Training and grading a 85 element optimized norm-conserving pseudopotential table, Comput. Phys. Commun. 226 (2018) 39–54. doi:10.1016/

j.cpc.2018.01.012.
[51] N. Marzari, D. Vanderbilt, Maximally localized generalized Wannier functions for composite energy bands, Phys. Rev. B 56 (1997) 12847–12865. doi:10.1103/PhysRevB.56.12847.
[52] I. Souza, N. Marzari, D. Vanderbilt, Maximally localized Wannier functions for entangled energy bands, Phys. Rev. B 65 (2001) 035109. doi:10.1103/PhysRevB.65.035109.
[53] V. Vitale, G. Pizzi, A. Marrazzo, J. R. Yates, N. Marzari, A. A. Mostofi, Automated high-throughput Wannierisation, npj Comput. Mater. 6 (1) (2020) 66. doi:10.1038/s41524-020-0312-y.
[54] A. Damle, L. Lin, L. Ying, Compressed representation of Kohn–Sham orbitals via selected columns of the density matrix, J. Chem. Theory Comput. 11 (4) (2015) 1463–1469. doi:10.1021/ct500985f.
[55] A. Damle, L. Lin, Disentanglement via entanglement: A unified method for Wannier localization, Multiscale Model. Simul. 16 (3) (2018) 1392–1410. doi:10.1137/17M1129696.
[56] Q. Wu, S. Zhang, H.-F. Song, M. Troyer, A. A. Soluyanov, WannierTools: An open-source software package for novel topological materials, Comput. Phys. Commun. 224 (2018) 405–416. doi:10.1016/j.cpc.2017.09.033.
[57] T. Miyasato, N. Abe, T. Fujii, A. Asamitsu, S. Onoda, Y. Onose, N. Nagaosa, Y. Tokura, Crossover behavior of the anomalous Hall effect and anomalous Nernst effect in itinerant ferromagnets, Phys. Rev. Lett. 99 (2007) 086602. doi:10.1103/PhysRevLett.99.086602.
[58] A. Miura, H. Sepehri-Amin, K. Masuda, H. Tsuchiura, Y. Miura, R. Iguchi, Y. Sakuraba, J. Shiomi, K. Hono, K.-i. Uchida, Observation of anomalous ettingshausen effect and large transverse thermoelectric conductivity in permanent magnets, Applied Physics Letters 115 (22) (2019) 222403. doi:10.1063/1.5131001.
[59] A. Sakai, Y. P. Mizuta, A. A. Nugroho, R. Sihombing, T. Koretsune, M.-T. Suzuki, N. Takemori, R. Ishii, D. Nishio-Hamane, R. Arita, P. Goswami, S. Nakatsuji, Giant anomalous Nernst effect and quantum-critical scaling in a ferromagnetic semimetal, Nat. Phys. 14 (11) (2018) 1119–1124. doi:10.1038/s41567-018-0225-6.
[60] R. Ramos, M. H. Aguirre, A. Anadón, J. Blasco, I. Lucas, K. Uchida, P. A. Algarabel, L. Morellón, E. Saitoh, M. R. Ibarra, Anomalous Nernst effect of fe_3o_4 single crystal, Phys. Rev. B 90 (2014) 054422. doi:10.1103/PhysRevB.90.054422.
[61] N. Hanasaki, K. Sano, Y. Onose, T. Ohtsuka, S. Iguchi, I. Kézsmárki, S. Miyasaka, S. Onoda, N. Nagaosa, Y. Tokura, Anomalous Nernst effects in pyrochlore molybdates with spin chirality, Phys. Rev. Lett. 100 (2008) 106601. doi:10.1103/PhysRevLett.100.106601.
[62] J. Weischenberg, F. Freimuth, S. Blügel, Y. Mokrousov, Scattering-independent anomalous Nernst effect in ferromagnets, Phys. Rev. B 87 (2013) 060406. doi:10.1103/PhysRevB.87.060406.
[63] Y. Pu, D. Chiba, F. Matsukura, H. Ohno, J. Shi, Mott relation for anomalous Hall and Nernst effects in $Ga_{1-x}Mn_xAs$ ferromagnetic semiconductors, Phys. Rev. Lett. 101 (2008) 117208. doi:10.1103/PhysRevLett.101.117208.
[64] M. Ikhlas, T. Tomita, T. Koretsune, M.-T. Suzuki, D. Nishio-Hamane, R. Arita, Y. Otani, S. Nakatsuji, Large anomalous Nernst effect at room temperature in a chiral antiferromagnet, Nat. Phys. 13 (11) (2017) 1085–1090. doi:10.1038/nphys4181.
[65] X. Li, L. Xu, L. Ding, J. Wang, M. Shen, X. Lu, Z. Zhu, K. Behnia, Anomalous Nernst and righi-leduc effects in mn_3Sn: Berry curvature and entropy flow, Phys. Rev. Lett. 119 (2017) 056601. doi:10.1103/PhysRevLett.119.056601.
[66] Y. Hirokane, Y. Tomioka, Y. Imai, A. Maeda, Y. Onose, Longitudinal and transverse thermoelectric transport in MnSi, Phys. Rev. B 93 (2016) 014436. doi:10.1103/PhysRevB.93.014436.
[67] S. N. Guin, P. Vir, Y. Zhang, N. Kumar, S. J. Watzman, C. Fu, E. Liu, K. Manna, W. Schnelle, J. Gooth, C. Shekhar, Y. Sun, C. Felser, Zero-field Nernst effect in a ferromagnetic Kagome-Lattice Weyl-Semimetal $Co_3Sn_2S_2$, Adv. Mater. 31 (25) (2019) 1806622. doi:10.1002/adma.201806622.
[68] H. Yang, W. You, J. Wang, J. Huang, C. Xi, X. Xu, C. Cao, M. Tian, Z.-A. Xu, J. Dai, Y. Li, Giant anomalous Nernst effect in the magnetic Weyl semimetal $Co_3Sn_2S_2$, Phys. Rev. Mater. 4 (2020) 024202. doi:10.1103/PhysRevMaterials.4.024202.
[69] L. Xu, X. Li, L. Ding, T. Chen, A. Sakai, B. Fauqué, S. Nakatsuji, Z. Zhu, K. Behnia, Anomalous transverse response of Co_2MnGa and universality of the room-temperature $\alpha_{ij}^A/\sigma_{ij}^A$ ratio across topological magnets, Phys. Rev. B 101 (2020) 180404. doi:10.1103/PhysRevB.101.180404.
[70] V. K. Jain, N. Lakshmi, V. Jain, A. K. Sijo, K. Venugopalan, High energy ball milling study of Fe_2MnSn Heusler alloy, in: AIP Conf. Proc., Vol. 1665, AIP Publishing, 2015. doi:10.1063/1.4918180.
[71] K. H. J. Buschow, P. G. Van Engen, R. Jongebreur, Magneto-optical properties of metallic ferromagnetic materials, J. Magn. Magn. Mater. 38 (1) (1983) 1–22. doi:10.1016/0304-8853(83)90097-5.
[72] The crystal structure of Ni-doped Co_3Sn is usually called as DO_3, which is a sepcial case of $L2_1$.
[73] G. K. Shukla, J. Sau, N. Shahi, A. K. Singh, M. Kumar, S. Singh, Anomalous Hall effect from gapped nodal line in the Co_2FeGe Heusler compound, Phys. Rev. B 104 (2021) 195108. doi:10.1103/PhysRevB.104.195108.
[74] J.-C. Tung, G.-Y. Guo, High spin polarization of the anomalous Hall current in Co-based Heusler compounds, New J. Phys. 15 (3) (2013) 033014. doi:10.1088/1367-2630/15/3/033014.